Yttria Reinforced Fe-Cr Ferritic Alloy Based Nanocomposites for Fusion Reactor Structural Applications

Submitted in the partial fulfilment
of the requirements for the award of the degree
of

MASTER OF TECHNOLOGY

In

Materials Engineering

By

MOSES JP

DEPARTMENT OF METALLURGICAL AND MATERIALS
ENGINEERING

INDIAN INSTITUTE OF TECHNOLOGY, ROORKEE

ROORKEE – 247667 (INDIA)

MAY, 2018

CANDIDATE'S DECLARATION

I hereby declare that the proposed work presented in this dissertation entitled "**Yttria Reinforced Fe-Cr Ferritic Alloy Based Nanocomposites for Fusion Reactor Structural Applications**" in fulfilment of the requirements for the award of the degree of **Master of Technology** in **Metallurgical and Materials Engineering** with specialization in **Materials Engineering**, submitted in the **Department of Metallurgical and Materials Engineering, Indian Institute of Technology Roorkee** is an authentic record of my own work carried out during the period from July 2017 to May 2018 under the supervision of **Dr. Suhrit Mula**, Assistant Professor, Department of Metallurgical and Materials Engineering, Indian Institute of Technology Roorkee.

The substance presented in this dissertation has not been submitted by me anywhere in any form for awarding any degree.

Dated: 17-05-2018

Place: Roorkee

(MOSES JP)

CERTIFICATE

This is to certify that the above statement made by the candidate is correct to the best of my knowledge and belief.

(Dr. SUHRIT MULA)

Assistant Professor

Department of Metallurgical and Materials Engineering

Indian Institute of Technology Roorkee

Roorkee – 247667 (INDIA)

ACKNOWLEDGEMENT

IIT Roorkee

Date: 17-05-2018   (MOSES JP)

ABSTRACT

Ferritic steel with oxide dispersion strengthening (ODS) is a promising material for fusion and fission reactor components. In this study, the influence of Zr, V, Mo on yttria dispersed ferritic alloys was analysed. The powders were developed by using mechanical alloying (MA) and subsequently consolidated by spark plasma sintering (SPS) at different temperatures (900°C, 1000°C & 1050°C) in argon atmosphere. The densification of the alloys was found to improve significantly with increase in the sintering temperature. The maximum relative density was found to be 97.5-98.3% with samples sintered at 1050°C. Microstructural analyses, carried out by optical and scanning electron microscopy (SEM), showed random orientation of grains with bimodal grain size distribution. X-ray diffraction phase analysis showed the presence of bcc ferritic phase in which Y-Ti-O, TiO and Ti-Cr-O oxides were dispersed and this was confirmed through transmission electron microscopy (TEM). Further, the hardness value obtained by nanoindentation was correlated with the compressive strength and wear resistance. The results have been analysed in terms of alloying and strengthening mechanisms.

Keywords: Mechanical alloying, spark plasma sintering, compression test, nanoindentation wear resistance.

TABLE OF CONTENTS

LIST OF FIGURES

LIST OF TABLES

CHAPTER 1   INTRODUCTION

Fast breeder generation IV nuclear reactors is a major step towards an efficient source of energy without affecting the surrounding environment by reducing the waste production and better safety controls [1]. The efficiency as well as safety of the fusion reactor depends upon some critical parts such as cladding tubes, first wall, diverter, limiters, and breeding blanket. These critical components, in addition to the high radiation dose produced by the neutron reactive environment should also withstand the stresses produced by strong mechanical, thermal and electromagnetic loadings. Due to this, materials used for designing nuclear reactor application must have adequate properties such as strength, ductility, creep resistance, fatigue strength, toughness and low radiation-induced swelling [2]. Although austenitic steel has high strength compare to ferritic materials, austenitic steels are not suitable for nuclear structural applications due to its huge loss of ductility and high swelling rate under irradiation of neutrons [3]. Fe-Cr based ferritic alloys are widely used as base materials in fusion reactors, with Cr content more than 12.7wt% to avoid transformation to FCC structure at higher temperature and has low vulnerability to transformation under neutron irradiation environment. Since these materials are to be used in the applications where the service temperature is high, the grain stability is a property which cannot be compromised. By the addition of elements like yttrium[4] and hafnium[5] to the Fe-Cr system effectively stabilize the growth of grains even in higher temperature. Though high Cr ferritic steels have remarkable properties for resisting corrosion and oxidation, with addition of rare-earth oxides such as Y_2O_3 or CeO gives excellent strength and creep resistance in elevated temperature. Oxide dispersion strengthened (ODS) ferritic material was found to be a promising candidate for structural applications in fusion reactors[6]. When these oxides are in nanoscale size, they exhibit enhanced mechanical properties and excellent radiation stability because of its larger interfacial areas acting as sink for irradiation induced helium atoms and vacancies[7]–[9]. Recent research reported that Y_2O_3 reinforced ferritic alloys show excellent creep resistance compare to non-ODS steels[10] and also much stable under radiation environment than compare to other oxides such as MgO, Al_2O_3[11]. S. Ukai et.al [12] reported that Ti has the tendency to refine the yttria oxide particles, when it is added to ferritic matrix, thus produces fine Y-Ti-O complex oxide after adequate milling and heat treatment. Additionally, Ti plays a positive role, when there is excess oxygen content which arose during milling, by increasing the hardness of the material [13]. These complex oxides which were formed due to the addition of Ti were reported to be less than 10nm in size [14], consequently increasing the creep resistance of the material drastically [12].

One of the common processing method of obtaining these ODS alloys is by powder metallurgy process, in which nanocrystalline powder particles are obtained by ball milling and further consolidated into solids by different high-temperature sintering processes. Recent development in ODS steel design led to two main options for base materials (i) on the basis of workability, 9-12Cr ODS ferritic/martensitic steel is wildly selected due to the allotropic cold work transformation of α-to-γ phase which can be transformed into novel isotropic recrystallized microstructure. (ii) 14Cr ODS fully ferritic steels because on their enhanced corrosion resistance property offered by high chromium content and tougher microstructure due to the absence of allotropic transformation. The process of consolidating the milled powders to bulk sample was tried using different sintering techniques like, cold compaction and pressure-less sintering[15], hot extrusion[16], equi-channel angular pressing [17][18], high pressure sintering[17][18], hot isostatic pressing [11], laser sintering [21] and spark plasma sintering[22]–[25]. Spark Plasma Sintering (SPS) is a recently developed technology, which is considered to give the best compacting properties compare to other sintering processes. In SPS, due the presence of both pressure and electric field-assisted consolidation (generation of plasma), powders directly heated up by a high current intensity and combines with other particles due to formation of necks by bulk and surface diffusion. This allows in the reduction of overall consolidation time and thus reduces the chances of rapid grain growth while sintering in conventional methods. Research works dealing with consolidating the ODS ball-milled powders through SPS process is not extensively studied.

The composition of ferritic steel itself need to be optimized on the basic of physical and mechanical properties in both ambient and high temperature irradiation conditions. In the present study, the base composition was taken similar to MA957 (Fe-14%Cr-1%Ti-0.3%Mo-0.25%Y_2O_3) which is commercially used in fusion reactor applications[26]. The effect of Zr, V instead of Mo in MA957 was studied after sintering the mechanically alloyed powders by SPS process. Temperature of sintering was optimized with respect to densification of the consolidated products. The microstructural evolution on these alloys at different sintering temperatures was studied and correlated with properties such as hardness, compression strength and resistance to wear for the corresponding sample.

CHAPTER 2   LITERATURE REVIEW

2.1 Requirements of Materials used in Fusion Reactors

Materials for nuclear reactors should endure the effects of high irradiation in both room and elevated temperature. These materials must withstand in this harsh environment for a prolong time period in high pressures condition[27].

The major requirements that a material should have if it can sustain the nuclear reactor environment are

a) Enhanced mechanical properties such as structural strength, hardness, wear resistance and creep resistance.

b) Low absorption of neutrons so that the material will have high radiation stability under strong gamma and neutron irradiation.

c) Corrosion resistance should be high since these materials will be exposed to fuel cell environment for a long period which is highly reactive thus causes corrosion.

d) Good thermal stability since these materials will be exposed to high temperature environment it can undergo thermal expansion which can alter the material properties as well as hinder other components near to it [28].

Intense research and experiments was done to find the materials which can sustain all this properties, which has led to some promising candidate materials for fusion reactor applications.

Ferritic/martensitic steels: Ferritic-martensitic steels with 9–12% Cr are used in lead or sodium cooled reactors whose working temperature is above 875 K. Due to their BCC structure these materials will have high swelling resistance, addition to this martensitic microstructure gives these materials the ability to have high density of sinks due to which they have negligible hardening and embrittlement when kept at irradiation environment even at 675–825K [29].

Oxide dispersion strengthened steels: The use of Oxide dispersion strengthened steels are now considered for the applications like cladding elements in high burn-up fast neutron reactor fuels. Through recent research it was observed that dispersion of nanosize dispersoids in ferritic matrix has significantly increased the creep [30] and wear resistance [31] of the material.

Ceramic materials: Component which are exposed to very high temperature in the range of 1275K, such as heat exchanger and primary thermal insulation systems, constituents in fuel and control rod systems, need excellent thermal stability. Ceramics due to its high melting temperature stands as the ideal candidate for this applications. Unfortunately, ceramic materials are known for its oxidation behavior at temperatures above 1300K and their behavior under irradiation could be a real problem due to its risk in swelling and loss in thermal conductivity[32].

Nickel Based alloys: Nickel based alloys such as Haynes 230, Inconel 617 were used in high temperature systems such as intermediate heat exchangers and critical components of turbines. These alloys exhibit good stability under thermal cycle over a long period, moderate creep resistance and have a well-established welding and metal working techniques. Corrosion resistance of Inconel 617 alloys are poor [33], [34] that compare to other alternative materials because non protective oxide layers are formed which lead to decarburization and internal corrosion. Moreover, high Co content present in these alloys presents a potential radioactive contamination problem.

2.2 Oxide Dispersion Strengthened (ODS) Alloys

In ODS steels due to the obstruction in movement of dislocation and grain stability obtained by nanosized dispersoids, these materials show excellent creep resistance in elevated temperature also[35]. Dispersoids exerts pinning force to hinder the movement of grain boundary. Although Austenitic steel has high strength compare to ferritic materials but due it's to high swelling rate and huge loss of ductility under irradiation of neutrons, austenitic steels are not preferred in nuclear applications[36]. Ferritic-martensitic steels with 9–12%Cr were found to be the ideal candidates for construction of in-core and out-of-core in the next generation of fission nuclear reactors[37], but this steels are not stable at higher temperature due to their phase transformation at elevated temperature.

Garner et al.,[38] compared swelling and creep resistance of BCC ferritic steel and FCC austenitic steel in high irradiation atmosphere and found that swelling Resistance of ferritic is more due to BCC structure and the thermal stability due to absence of phase change promotes ferritic as the promising candidate. From **Fig. 1** it is seen clearly that with increase in chromium content the amount of swelling drastically decreases. If chromium content is more than 14% then the materials can escape the austenitic loop at elevated temperature, i.e. there won't be any phase transformation at higher thermal thus offers an excellent thermal stability.
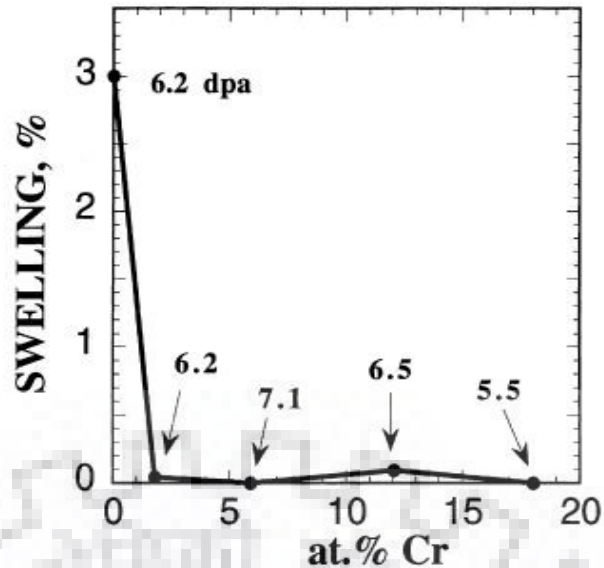
Fig. 1 Influence of Cr in controlling swelling [38]

Addition of Ti enhances the mechanical properties of the steel. Ukai et al.,[39] reported this superior effect of addition of Ti in the ODS ferritic steel, it was found that Ti act as a refiner to produce Y-Ti-O oxides in presence of yttria which act as excellent creep resistance. Sakasegawa et.al.,[14] found the size of this Y-Ti-O oxide particles was in the range of 2-5nm by TEM analysis (as shown in **Fig. 2**) when 0.4%Ti was added to 12YWT steels.
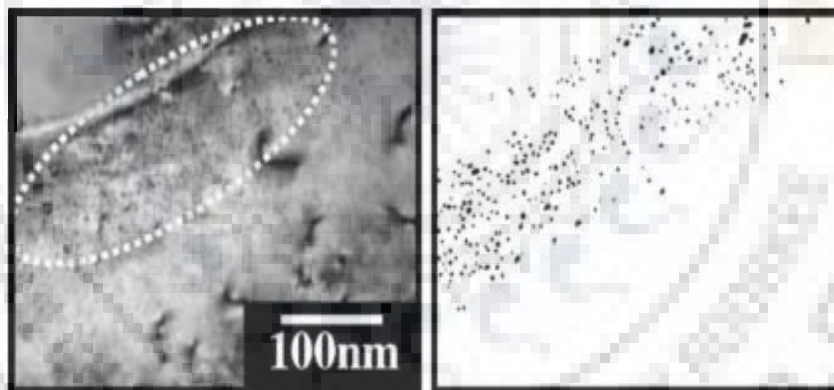
Fig. 2 TEM image shows the presence of Y-Ti-O [14]

Odette et.al.,[40] found that addition of yttria in ferritic steel act as grain growth stabilizer by giving zinner pining in higher temperature. Addition of yttria enhanced the mechanical properties by (i) pinning the dislocation movement (ii) Stable sink for irradiation induced defect (iii) Nucleation sites for small helium bubbles. Cayron et.al.,[41] reported the stability of Y_2O_3 over other oxide particles such as MgO, Al_2O_3. In their research Y_2O_3 was found to be less unstable oxide under irradiation by neutron, electron and ions compare to other oxides. Ukai et.al.,[10] studied the effect of yttria in Fe-9Cr steel and found that creep resistance was increased about three times greater than non ODS alloys.

Sakasegawa et al[42] studied the chemical composition and thermal stability of the oxides formed in MA957 and reported that there were two type of phases 1) Non-Stoichiometric nanoclusters size ranging from 2-15nm 2) Stoichiometric nanoclusters size ranging 15-35nm as mentioned in **Fig. 3**. It was also suggested that changing Ti and Yttrium content can effectively modify the fine dispersion of oxides. It was observed that Non-Stoichiometric particles gives more strengthening that Stoichiometric particles due to their smaller size they have good coherence with the matrix interface and also hinders in dislocation motion. When the material is annealed at 1200°C for 1h, some non-Stoichiometric start to grow due to Ostwald ripening (by diffusion of Yttrium).
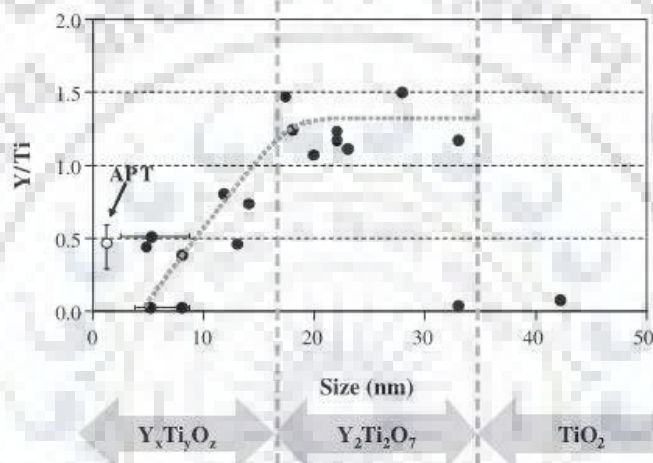
Fig. 3 Size range of various oxides vs Y/Ti ratio [42]

It was revealed by Ohtsuka et al.,[13], that the merely increasing Y_2O_3 and Ti addition (as shown in **Fig. 4**) cannot improve the high-temperature strength. The excess oxygen is defined as the subtracting oxygen content in yttria from total oxygen in present in the alloy steel. The excess oxygen is an important parameter for making oxide particles finely and densely distributed as well as improving high-temperature strength.
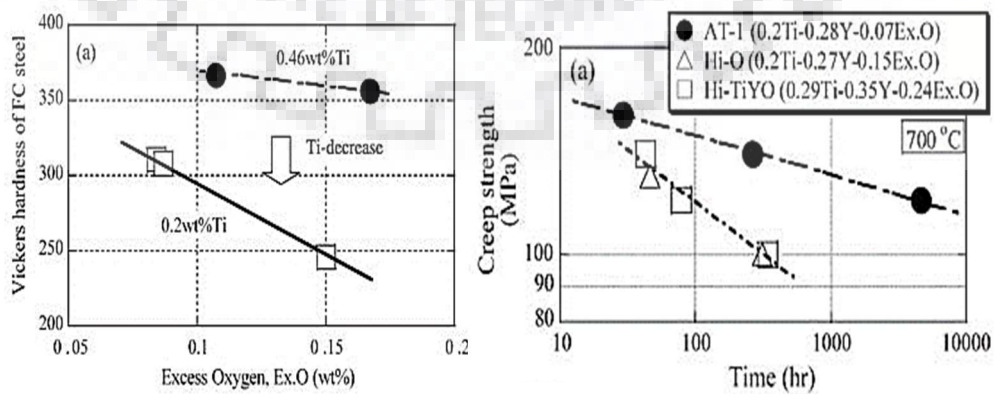
Fig. 4 Change in properties with excess oxygen content [13]

6

Okuda et. al,[43]. reported the size distribution of various oxides forming in Fe-12Cr ODS steel. The addition of Ti, Nb, V, Zr with yttria produces complex oxide particles in the size varying from 2-20nm. Y-Ti-O oxide was found to have less size compare to other oxide particles. **Fig. 5** shows the size of oxide particles obtained by adding different elements.
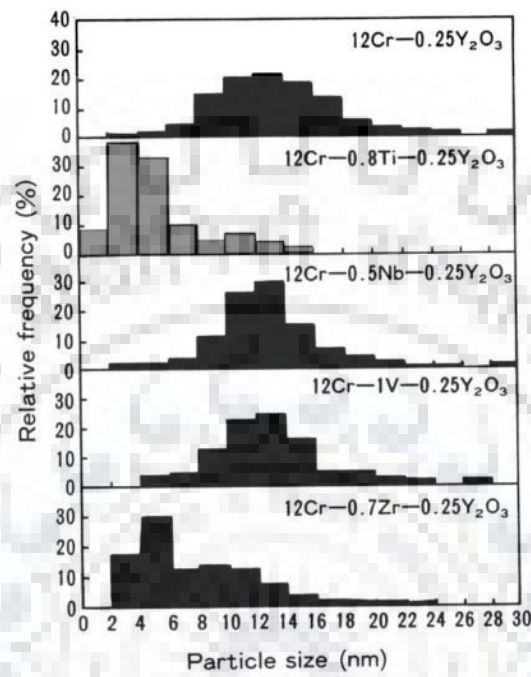
Fig. 5 Oxide size histogram by TEM analysis due to addition of various element [43]

Karak et al.[31], investigated the change in wear behavior of yttria dispersed ferritic steel system. Addition of yttria was found to give maximum wear resistance with 1 wt% nano yttria sintered at 1000°C by hot isostatic pressing. It was also found that the presence of Y-Ti-O enhanced the wear properties compare to the non ODS ferritic alloys (as mentioned in **Fig. 6**).
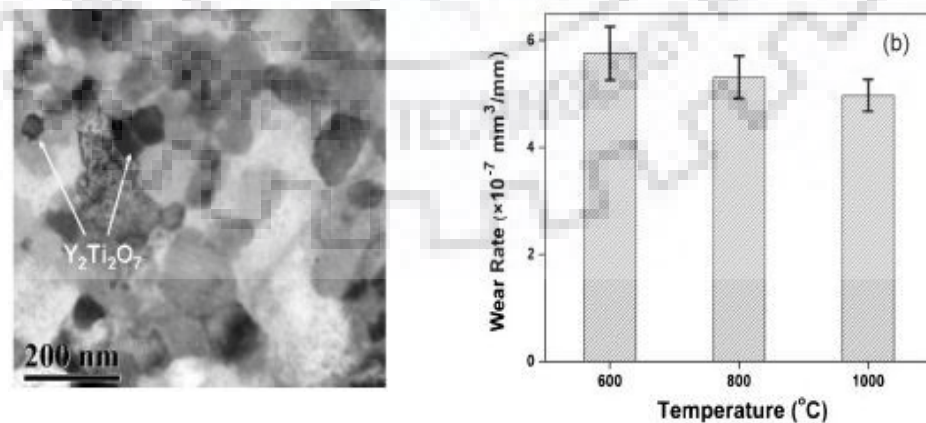
Fig. 6 (a)Presence of complex oxides at 1000°C (b)Wear rate vs sintering temperature [31]

2.3 Mechanical Alloying

Mechanical alloying (MA) is one of the solid-state powder processe which involves repeated cold welding, followed by fracturing, and again rewelding of powder particles in a high-energy ball mill. General outline of MA starts with blending powders with a required composition and milling it with a grinding medium with a high energy ball mill for desired duration of period, until the composition of milled powder particle is similar to the proportion of powder particle before milling. The milled powder is then sintered into a required shape at higher temperature to obtain the desired properties and microstructure.

Suryanarayana et al. [44] explain that the non-equilibrium conditions can control the structure and constitution of the material in a better way, which makes them to give precise properties for demanding applications. Commercially used processes to develop advanced materials include rapid solidification from liquid state, mechanical alloying, plasma processing and vapour deposition. **Fig. 7** shows non-equilibrium state by energizing and quenching of materials, by applying dynamic forces via externally through application of pressure, melting, irradiation, storing of mechanical energy by plastic deformation.
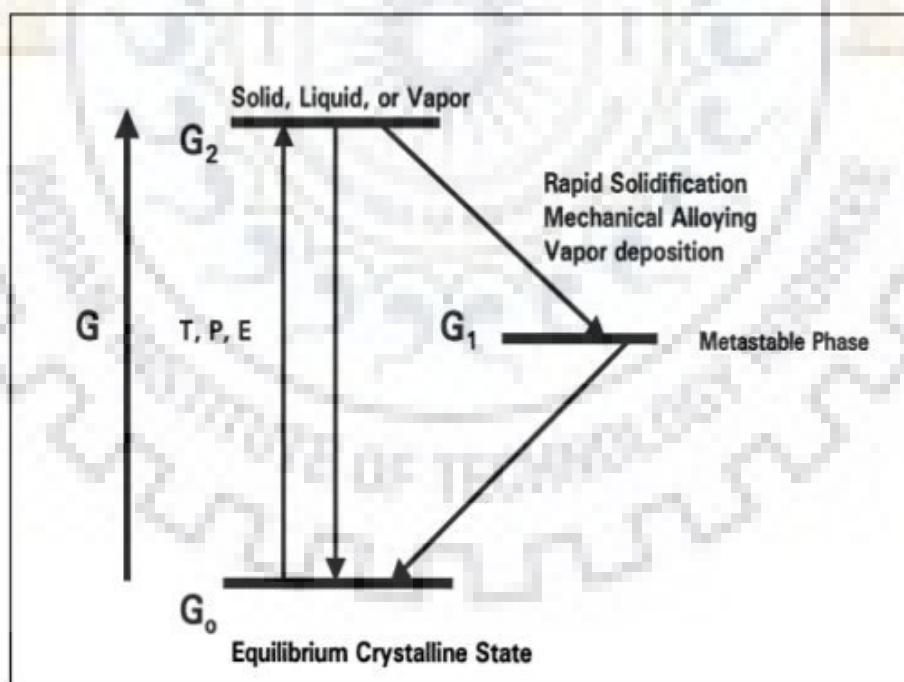
Fig. 7 The basic theory of "energize and quench" to produce non-equilibrium materials [44]

The important modules of the mechanical alloying process are raw materials, mill, and process variables. These powders have particle size in the range 1-200µm. The milling process is further referred as wet grinding or dry grinding depending upon whether a liquid medium is

used or not [45][46]. To obtain finer particle size wet grinding is preferred over dry grinding as the solvent molecules in wet grinding are adsorbed on the powder particle which results in lowering their surface energy[47]. Although wet grinding is advantageous in effective reduction of particle size, the major drawback is the contamination of the powder. Hence most mechanical alloying and mechanical milling processes have been carried out dry[44]. Different types of mills are used for mechanical alloying such as SPEX mills, planetary ball mills, attritor mills, Commercial mills etc., of these, planetary ball mill is one of the popular mill used for mechanical alloying. In a planetary ball mill few hundred grams can be milled at a time. Vials in a planetary ball mill are organized on a rotating support disk and a drive mechanism causes them to rotate around their own axes. The centrifugal force produced by the vials rotating around their own axes and that created by the rotation of support disk both contribute to vial constituents, consisting of material to be milled and the grinding balls[44].
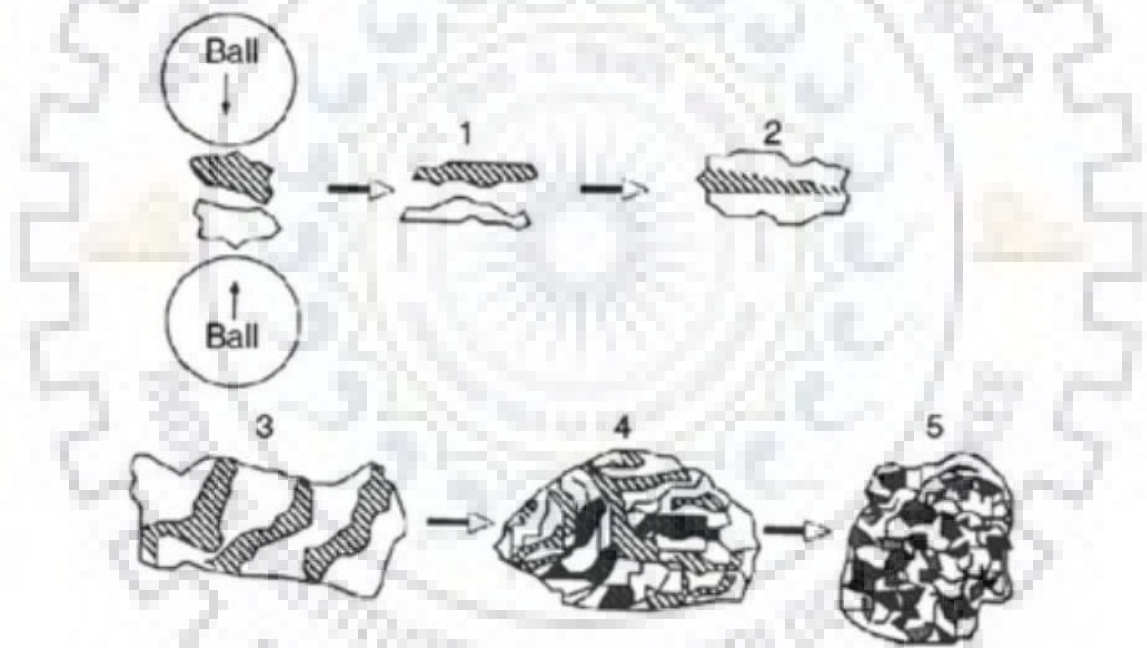
Fig. 8 Steps of powder evolution during mechanical alloying [48]

The actual process of MA starts with mixing of the powders in the right proportion and loading the powder mix into the mill along with the grinding medium. This mix is then milled for the desired length of time until a steady state is reached when the composition of every powder particle is the same as the proportion of the elements in the starting powder mixture. The milled powder is then consolidated into a bulk shape and heat treated to obtain the desired microstructure and properties [47]–[49]. **Fig. 8** shows the mechanism of alloying during via mechanical alloying. During high-energy milling the powder particles are subjected to repeated

flattening, cold welding, fracturing and rewelding to produce quality powders with controlled microstructure. The collisions occur between ball-powder, ball-ball and ball-vial. When two balls collide, some amount of powder is trapped in between them. The impacted force plastically deforms the powder particles leading to work hardening and fracture. In case of ductile materials, the powder got flattened and work hardened. Some new surfaces created by fracture and are able to weld together and this causes the increase in particle size and particle size as large as three times larger than the initial particles can be produced. The particles get work hardened and fractured due to continuous deformation by fatigue failure. After that the particle size will get reduced by the absence of agglomeration [50]. Further application of forces fracture predominates over cold welding. Due to the continued impact of grinding balls, the structure of the particles is steadily refined, but the particle size continues to be the same. During MA, heavy plastic deformation is introduced into the particles due to the high energy milling. This deformation causes crystal defects such as vacancies, dislocations, stacking faults and increased grain boundaries area.

2.4 Sintering Process

Sintering is carried out to increase strength and hardness of a green compact and consists of heating the compact to some temperature under controlled conditions with or without pressure for a definite time. Sintering process concerns with three main steps:

Diffusion: This takes place especially on the surface of the particles at elevated temperature[51]. Nanostructures obtained by mechanical alloying promote the diffusion process by increasing the surface area required for diffusion.

Densification: This decreases the porosity present in the green compact and increase the particle contact area. Due to this effect compact size decreases but this may not occur uniformly because of variations in the density of compact and hence distortions of component may arise.

Recrystallization and grain growth: This occurs between the particles at the contact area, leading to formation of the original one. The main driving force for sintering is the decrease in free energy due to decrease of surface area.

High performance applications require higher densities. Conventional methods leads to lower density products in compared with hot consolidation processes (hot pressing, HIP, spark plasma sintering, extrusion etc.) enable production of full-density or near full density powder materials/products [51][52].

Spark Plasma Sintering is a new technique which takes hardly few minutes to complete a sintering process compared to conventional sintering which may take hours or even days for the same. High sintering rate is possible in SPS [53][54]. The heating rates normally reached in conventional furnaces are 5 to 8 °C /min which can go maximum up to 10 °C /min. So, to reach a temperature of 1200 °C we usually need 2 to 4 hours or more whereas in SPS, heating rates exceeding 300 °C /min are easily obtained hence a temperature of 1200 °C can be obtained in only 4 minutes. In the presence of pressure and electric current, localized necking occurs faster due to joule heating as shown in **Fig. 9**. Consequently, the temperature rises very fast (faster than conventional sintering and Hot pressing) and the densification is completed within few minutes [55][56].
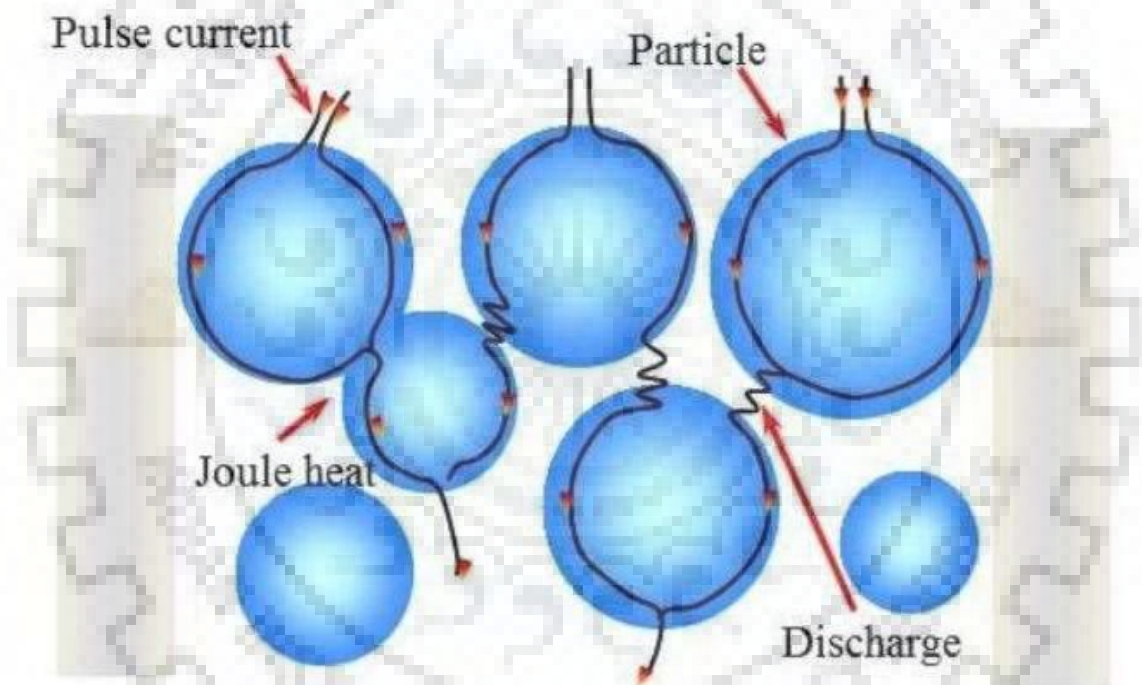
Fig. 9 Pulsed current path through the powders

With SPS technique one can easily achieve high densities, which are nearly comparable to theoretical density values due to application of temperature and pressure at same time, and lowers the sintering temperature range by 200-250 °C than in conventional process. Moreover, it avoids coarsening and grain growth which in-turn results in high densities [57][58]. This process has potential to use for powders with nano-size, nano-ceramics or nano composite these exhibits excellent mechanical properties like strength and hardness. High reactive materials can be easily sintered because of rapid heating and cooling cycle, and avoids formation of undesirable phases. When spark discharge appears in the gap between the particles of a material,

11

a local high temperature state occurs. This causes vaporization and melting which creates bond between the powder particles and narrow shapes or "necks" is formed around the contact area. These necks gradually grow and develop as diffusion progresses, resulting in a sintered compact of 99% density. Since only the surface temperature of the particles rises rapidly by self-heating, particle growth of the starting powder materials is controlled [59], [60].

2.5 Literature Summary

- Ferritic steel with 14% Cr is having more resistance to swelling under neutron radiation environment and also has enhanced thermal stability at higher temperature without undergoing any phase transformation.
- Addition of Y_2O_3 in the ferritic matrix gives good creep resistance and strength; it is also found to be stable under irradiation environment.
- When Ti is added with the presence of Y_2O_3, Ti has the tendency to reduce the oxide particles and form complex oxides of Y-Ti-O which will be in nanoscale.
- Addition of Ti also has a positive effect of increasing the strength of the material by forming TiO_2 with the excess oxygen formed during fabrication process.
- Through mechanical alloying, single phase solid solutions with grains size in nanoscale can be achieved.
- Sintered product with the help of SPS process can give enhanced mechanical properties by retaining the grain size in nanoscale regime due to less sintering time.

2.6 Literature Gaps

- Study on the effect of Mo, V, Zr on the 14%Cr ODS steels is not reported, though they have the tendency to form complex oxides.
- Study of sintering the ODS steels through SPS process is not widely explored.
- Wear behavior in ODS steels due to the presence of complex oxides as well as their behavior under compressive load is not widely described

2.7 Aims and objectives of the present study

The aims of the present work are as follows:

➢ To develop high strength ultra-fine grained Fe-Cr ODS alloys for high temperature applications such as nuclear, construction, petrochemical industries etc.

➢ To optimize the SPS sintering temperature of the 14%Cr ODS steels for fabrication of bulk sample which could provide close to theoretical density.

➢ To study the microstructural evolution and nature of oxide formation in the matrix.

➢ To investigate the mechanical properties, such hardness, compressive strength, elastic modulus of the sintered samples as function of sintering temperature. Correlation between the microstructure and mechanical properties will be established.
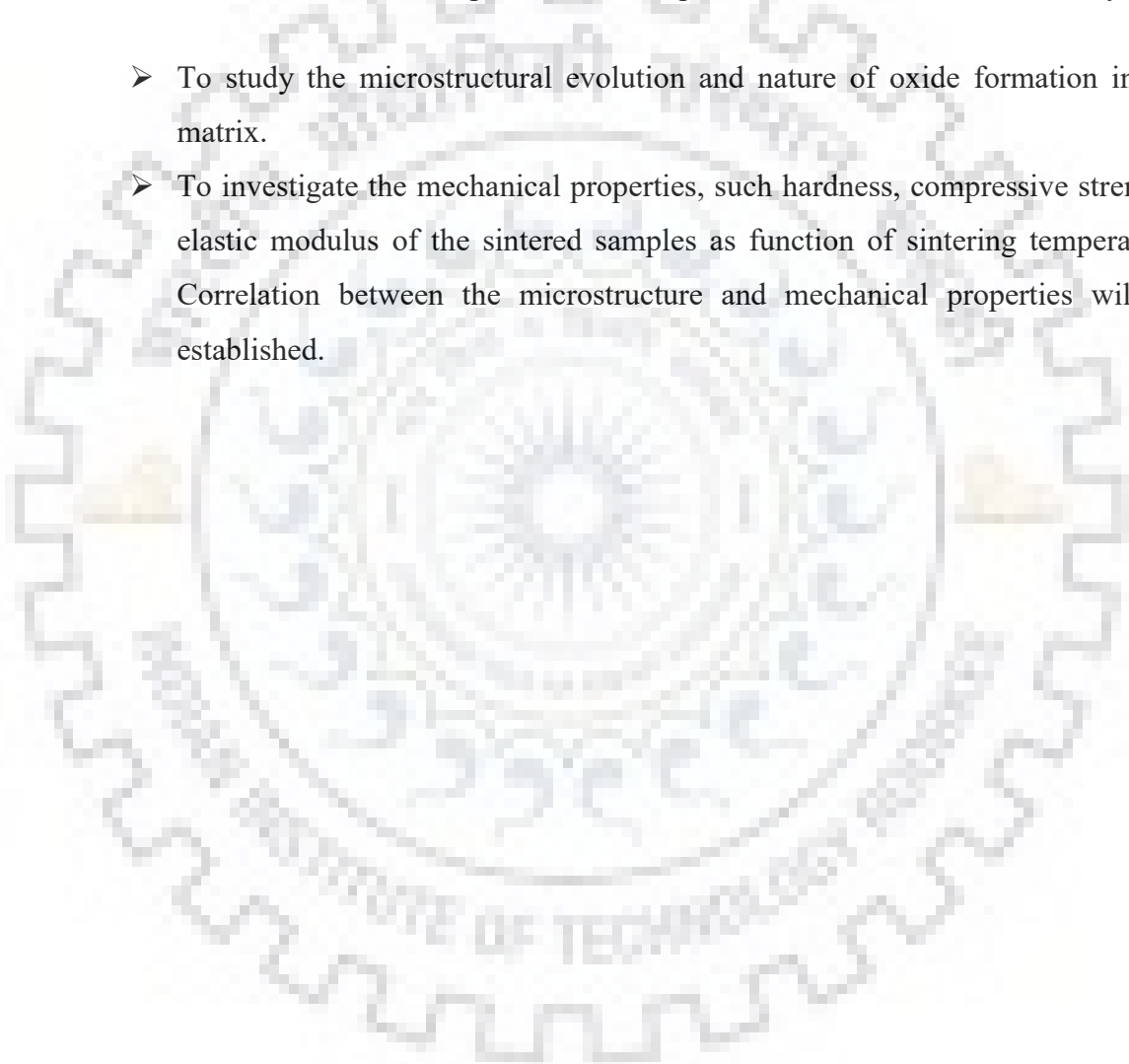
CHAPTER 3   EXPERIMENTAL PROCEDURE

3.1 Milling

3.1.1 Planetary ball milling

Pure yttria was milled in ball milling to reduce the size of the yttria to nano-metric level. As-received yttria powder was loaded to planetary ball milling (**Fig. 10)** in Tungsten carbide (WC) vial with a ball to powder ratio of 10:1 with toluene to reduce the milling temperature and avoid more oxidation while milling. The milling was carried out for 40h at 270 rpm, with an interval of 30min for every one hour of milling. Small amount of samples at 20h were taken to compare the variation in size of the milled powder with as-received and 40h milled sample.

Fig. 10 Planetary Ball Milling

3.1.2 High Energy Milling

High energy milling was carried out by SPEX 8000 (**Fig. 11**) by taking pure Fe, Cr, Ti, X(=Mo, Zr, V) with 40h milled yttria. The compositions were taken according to the following weight percentage combination Fe-14Cr-1Ti-0.3X-0.25Y_2O_3 (X=Mo, Zr, V) and milled for 25h in hardened stainless steel vail (440C grade) with stainless steel balls (17 in numbers of 8 mm diameter and 16 in numbers of 6 mm diameter). The milling was carried out with a ball to powder ration of 10:1 and in argon atmosphere. Milling temperature was controlled in 24°C by

controlling the room temperature. The milling was carried out with an interval of 20min for every 100 min of milling.

Table 1 Composition of the alloys

Alloy (wt%)	Fe	Cr	Ti	Y_2O_3	Mo	V	Zr
14CrYT-Mo	84.45	14	1	0.25	0.3	-	-
14CrYT-V	84.45	14	1	0.25	-	0.3	-
14CrYT-Zrf	84.45	14	1	0.25	-	-	0.3

Fig. 11 SPEX 8000 High Energy Milling

3.2 Spark Plasma Sintering (SPS)

The milled samples were sintered by SPS (Dr Sinter, SPS-625 Japan) at different temperatures 900, 1000 & 1050°C. The powder as weighed such that it would result in a sample size of 10mm diameter and 5mm thickness by correlating the density of the powder and the required volume of the sample. The samples were put in the graphite die and a layer of carbon film with boron nitride spray over this layer was done in the graphite die to avoid any sticking of sample with the punch and die. Then an axial pressure of 60MPa (4.7KN Load) was given to the sample to attain green compacting and the sintering chamber was filled with argon gas to avoid the chemical reaction of the powder samples with oxygen while sintering. The sample was sintered at a rate of 100°/min to the required temperature and 5mins holding time was given.

15
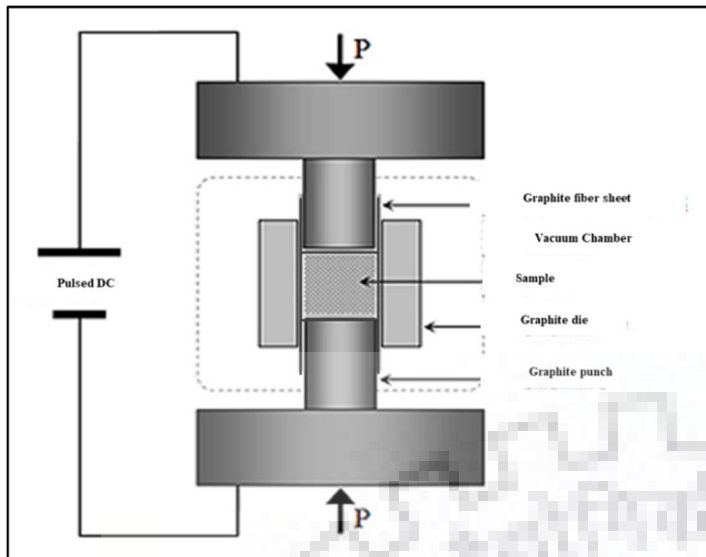
Fig. 13 Schematic diagram of SPS process
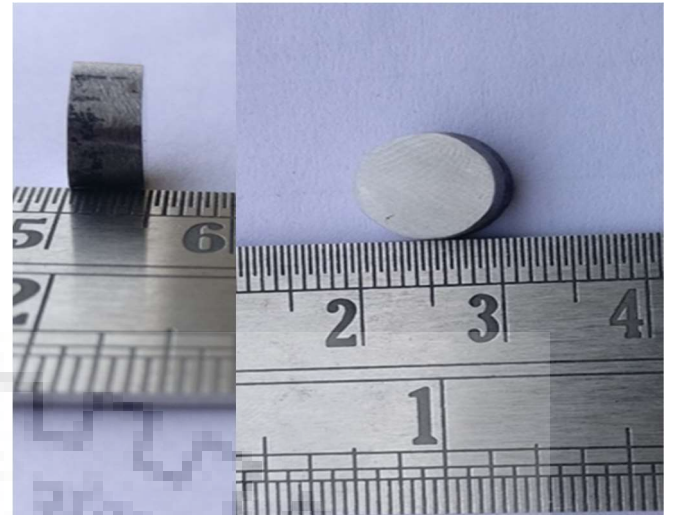
Fig. 12 SPS sintered samples

The temperature of the sample was measured by thermocouple which is having a physical contact with the graphite die. The temperature profile and the displacement of the anvil was automatically measured and plotted by the SPS instrument automatically. The pulse current was increased to 35% at the beginning to stabilize the voltage flow in the sample. The amount of displacement measure by the anvil of the punch in directly proportional to the density attained by the sample. After the holding time the sample was allowed to cool down and the dies was safely ejected by using hydraulic machine. Once the sample is ejected the outer carbon coating which was given initially was removed with the help of grinding machine or emery papers.

3.3 Density Measurement

Density of the sintered sample was measured by using Mettler Toledo weighing machine with density kit setup which uses Archimedes' principle to calculate the density of the material. The sample is first weighed in air and then weighed in distilled water. By the reduction in weight, the density of the sample is found out using Archimedes' principle. Each samples are tested 5 times after properly removing the moisture content in the sample. The relative density was found by dividing the density obtained during measurement to the theoretical density of the composition.

Fig. 14 Mettler Toledo weighing machine with density kit setup

3.4 XRD Analysis

Phases present in the milled powders and SPS sintered samples were found using X-ray diffraction (XRD) analysis. XRD was carried out using Co Kα (γ =0.1789 nm) radiation in Rigaku smart Lab X-ray diffractometer. X-Ray diffraction pattern were recorded from 20° to 120° with a step size of 0.02° at accelerating voltage of 40 kV. Data were collected with a scanning rate of 1°/min. C0 Kα$_2$ peak stripping and background subtraction were accomplished by using the X'pert HighScore Plus software.

Fig. 15 X-Ray Diffractometer

The average crystallite size was calculated by using scherrer equation (Eq.1) from after eliminating the broadening effects due to strain by annealing the powder samples up to 1100°C

with a heating rate of 5°C/min and holding it for 1h in tubular furnace. The annealing of the powder was done in Ar+2%H$_2$ atmosphere. During annealing all the strain induced during mechanical alloying due to sever plastic deformation was eliminated. After annealing, the powders are crusted manually by hand pulveriser and then used for XRD analysis. In SPSed samples, the surface of the samples was first cleaned to remove any impurities (such as carbon paper which was used during SPS sintering process) present in it.

$$t = \frac{0.9\lambda}{\beta\cos\theta} \qquad\qquad (1)$$

Where λ is the wavelength of the X-ray wavelength,

β is the line broadening at half the maximum intensity (FWHM), after subtracting the instrumental line broadening, in radians.

θ is the Bragg angle.

3.5 Optical Microscope

Microstructure of the SPSed samples were found using DM15000MTM Leica optical microscope, Switzerland. The samples were first polished with emery papers from grid size increasing from 320-2000, and finally the samples were cloth polished with alumina powder. The orientation of polishing was changed by 90° for each polishing stage. Then this polished samples was etched by using freshly prepared 10% nital solution for 50sec. This etched samples are then analyzed by optical microscope under magnification ranging from 100X to 1000X.

Fig. 16 Optical Microscopy

3.6 Scanning Electron Microscope

Field emission scanning electron microscopy (FE-SEM Model: ZEISS 51-ADD0048) was used to find the microstructure evolution of the sintered samples with respect to the increase in sintering temperatures. It is equipped with Oxford energy dispersive spectroscopy (EDS) system which was used for elemental analysis. The wear track was also analyzed using SEM for finding the wear width and also the nature of wear mechanism.

Fig. 17 Scanning Electron Microscope

3.7 Transmission Electron Microscope

Transmission electron microscope (FEI, Quanta 200F) was used to find the particle size of the milled powders and also to find oxide particles present in the SPSed samples. The powder samples were first ultra-sonicated with ethanol solution for 15mins to remove the agglomeration present in it. Then a drops of this mixture was dropped on to the 3 mm diameter carbon coated Cu-grid.

Fig. 18 Transmission Electron Microscope

For SPSed samples, the samples were reduced to <100μm thickness by using SiC abrasive papers. Then this samples was cut into 3mm disc and was dimpled to reduce the size to 30μm. This dimpled samples were loaded to Gatan Precision Ion Polishing machine system II at 6KV to get an ion thinned region for TEM analysis.

3.8 Nanoindentation

Nanoindentation test was done on the SPSed samples by Hysitron Nano Indenter (TI 950 TriboIndentor). Quasistatic Nanoindentation was used to measures the Young's modulus and hardness of the material via nanoindentation. Experiment was done with a loading rate of 100μN/s with a maximum load of 5000μN and with a holding time of 2sec at peak load. The SPSed samples were mirror polished, so that the indenter will not get affected by the roughness of the sample.
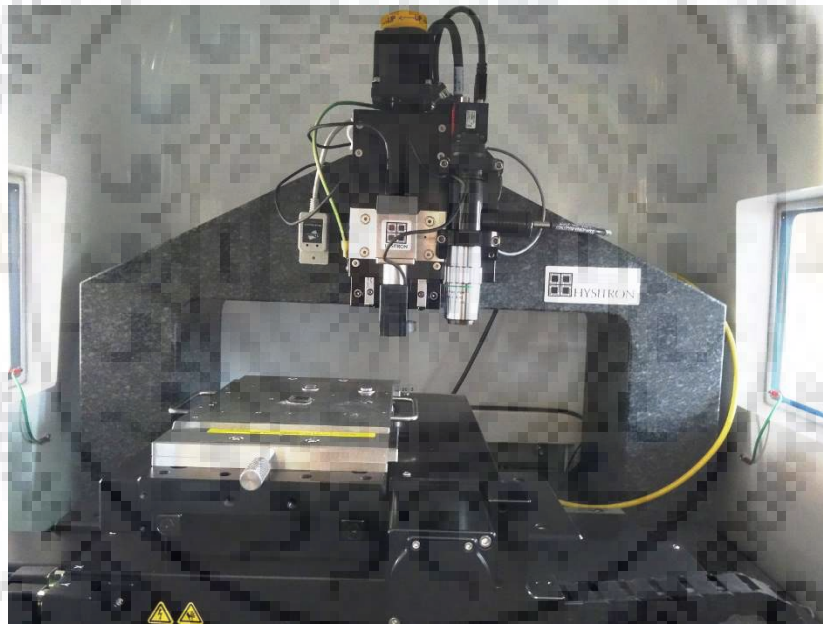
Fig. 19 Nanoindentation

3.9 Compression Test

Compression test was carried out in room temperature with universal testing machine (Hounsfield Model ZD-20). The compression test samples of dimension of 2mm X 2mm X 4mm size was prepared by cutting the SPSed samples through wire EDM machine. This samples were then loaded to the universal test machine by placing the test samples between tungsten carbide anvils as shown **Fig. 20**. Tungsten carbide anvils has very high hardness due to this it is used as base for testing specimen by which error occur due deformation can be neglected. The strain rate of the sample was maintained at strain rate of 1×10^{-3} s^{-1}.
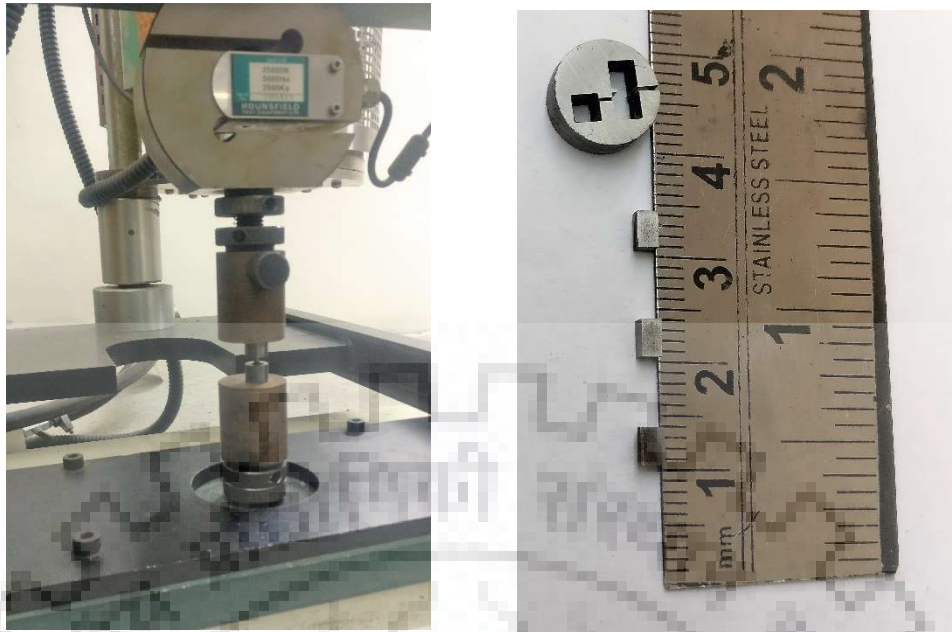
Fig. 20 a) Universal Testing Machine b)Compression test samples

3.10 Wear Test

Wear test on the samples which has higher density was carried out using DUCOM ball-on-disc sliding wear testing apparatus. A spherical single crystal alumina ball of diameter 10 mm and hardness of ~2000HV was used as a counter-body. Alumina ball was fixed stationary with the machine while sample was mounted on a circular plate which rotates at a constant speed of 500 rpm. The wear experiments were carried out at an ambient condition (at room temperature) in open air for 25 min. Three load (i.e. 5N, 10N, 20N) was used to find the change in wear behaviour of the sample will the application of load.
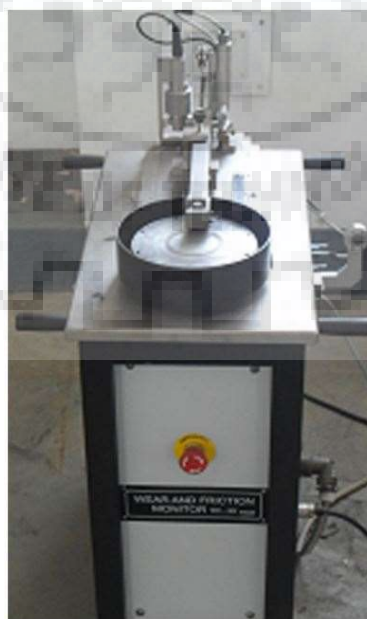
Fig. 21 Wear test machine

Coefficient of friction was found by the ratio between friction force and normal force. Electrical sensor was used to find and record the real time frictional force between the sample and single crystal alumina ball. The surface profile of the wear out specimens was found with the aid of Profilometer (SJ 400 Mitutoyo, Japan). For each sample, minimum 10 wear profiles were examined to acquire the average value of the wear depth of the wear surface.

3.11 Plan of work
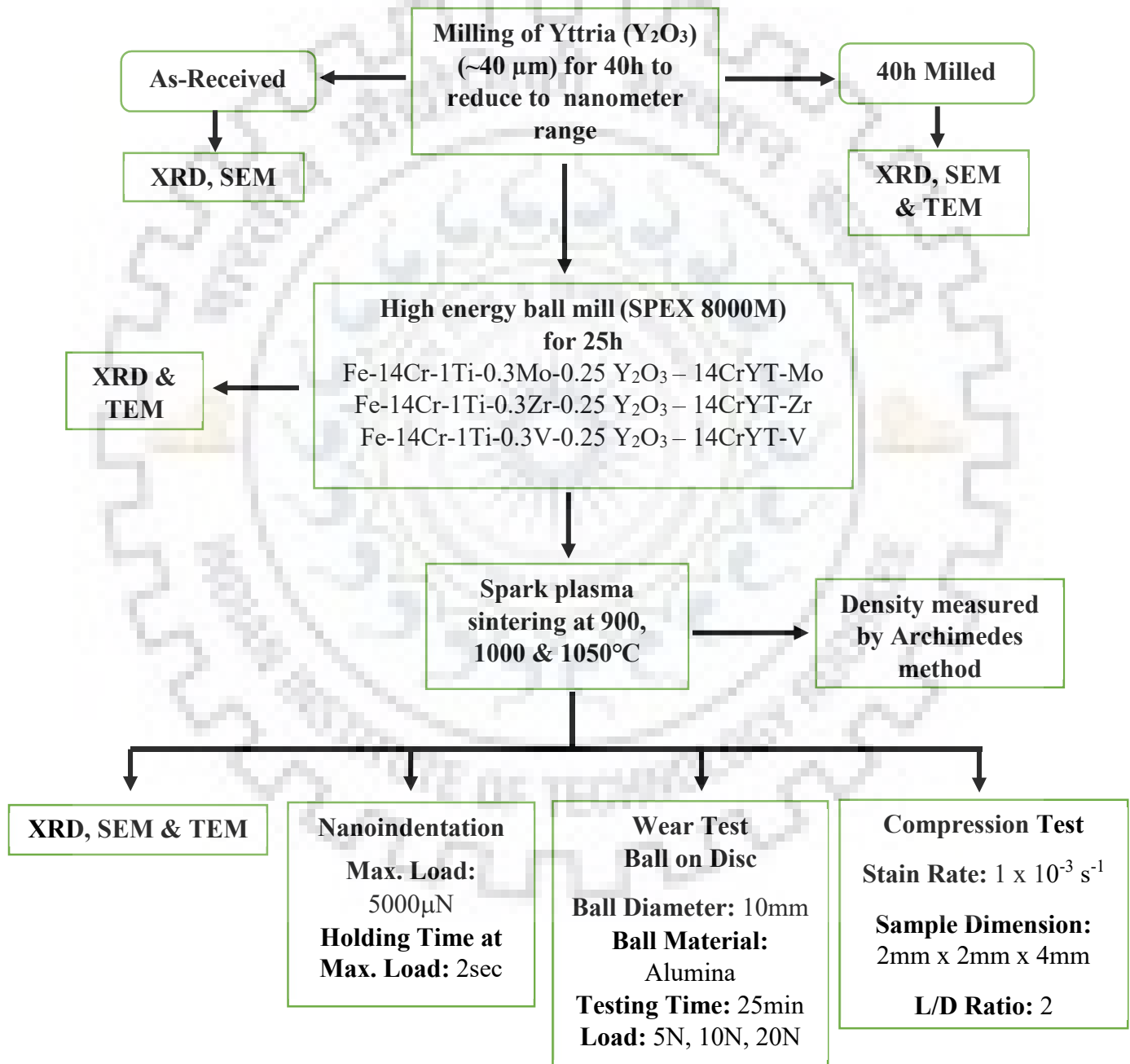
CHAPTER 4   RESULTS AND DISCUSSION

4.1 Milling of Yttria
4.1.1 XRD analysis

XRD analysis of the powder sample was carried out with Co as the target material and with a speed of 1°/min from 20° - 120°. **Fig. 22** shows comparison of the XRD analysis between as-received and 40h milled yttria powder. After milling XRD peak intensity got decrease and also broadened due to the particle size reduction and strain induced in the material while milling. Milling of yttria occurs due to brittle to brittle fracture mechanism. Since in milling, particles experience continuous welding and fracture which increases the strain in the material which shifts the angle towards left.
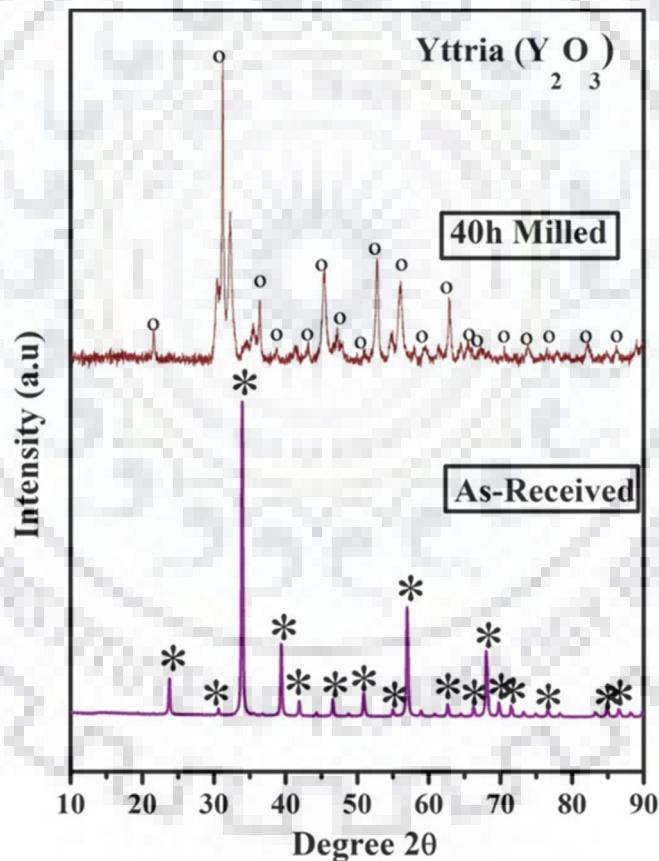
Fig. 22 XRD analysis of Milled - Pure Yttria

4.1.2 SEM analysis

Yttria powders where ultra-sonicated to break the agglomeration of powder particles. **Fig. 23** shows the reduction in size of yttria with increase in milling time. As-received powder had average size of 40μm and reduced gradually with increasing in milling time. The average size of

yttria at 20h and 40h were found to be 1μm and 10-20nm respectively. This reduction is due to the continuous plastic deformation and fracture of yttria particles while milling.
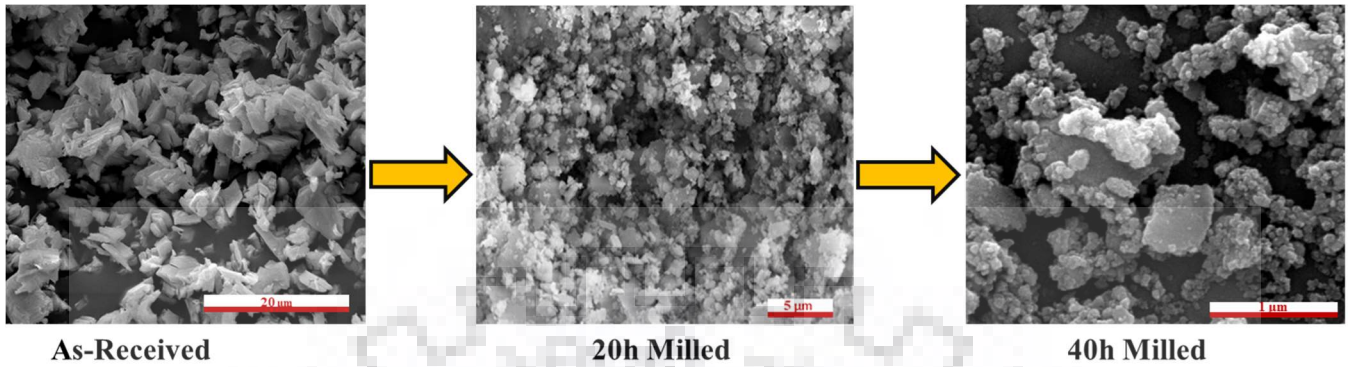
Fig. 23 SEM images of reduction in Yttria size

4.1.3 TEM analysis

TEM analysis was carried out on the 40h milled powder, from the **Fig. 24** it can clearly be seen that the size of the particles is in nano-metric size. This result is correlating with the result obtained through SEM analysis. The histogram shows that the size of the particles varies from 6nm – 25nm with any average size of 12.599nm obtained after 40h of milling.
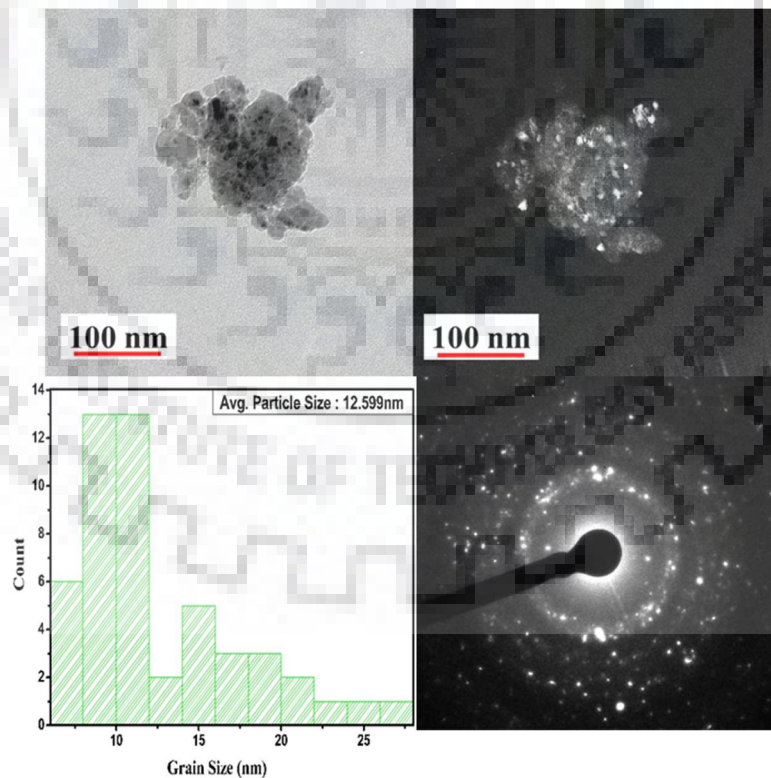
Fig. 24TEM images of 40h milled yttria powder a)Bright Field image b)Dark field image c)Particles size histogram d) SAED Pattern

4.2 Mechanical alloying
4.2.1 XRD analysis

Fig. 25 shows the XRD patterns in the range of 20° - 120° for various composition (14CrYT- Mo, V, Zr) milled for 25 h at room temperature. The peaks of other elements like Cr, Ti, Mo, V, Zr, Y_2O_3 are not detectable from the XRD analysis for all the compositions. This indicates complete dissolution of these elements in the in Fe-Cr matrix during 25 h of milling[4][61]. The formation of metallic oxides and intermetallic was not found in the as-milled powders, this might be due to the absence of these phases or the amount of these phases are in negligible amount. The shifting of peaks was found for all the compositions, this is due to the variation in the composition i.e. due to the addition of Mo, V, Zr. Addition of these elements can affect the lattice parameter of the solid solution due to which the peak shifts towards left [62]. It can be observed that the peak shift is high for V and reduces gradually in the order of Zr and Mo, which shows that addition of V has increased the lattice parameter of Fe more than compare to Mo and Zr.
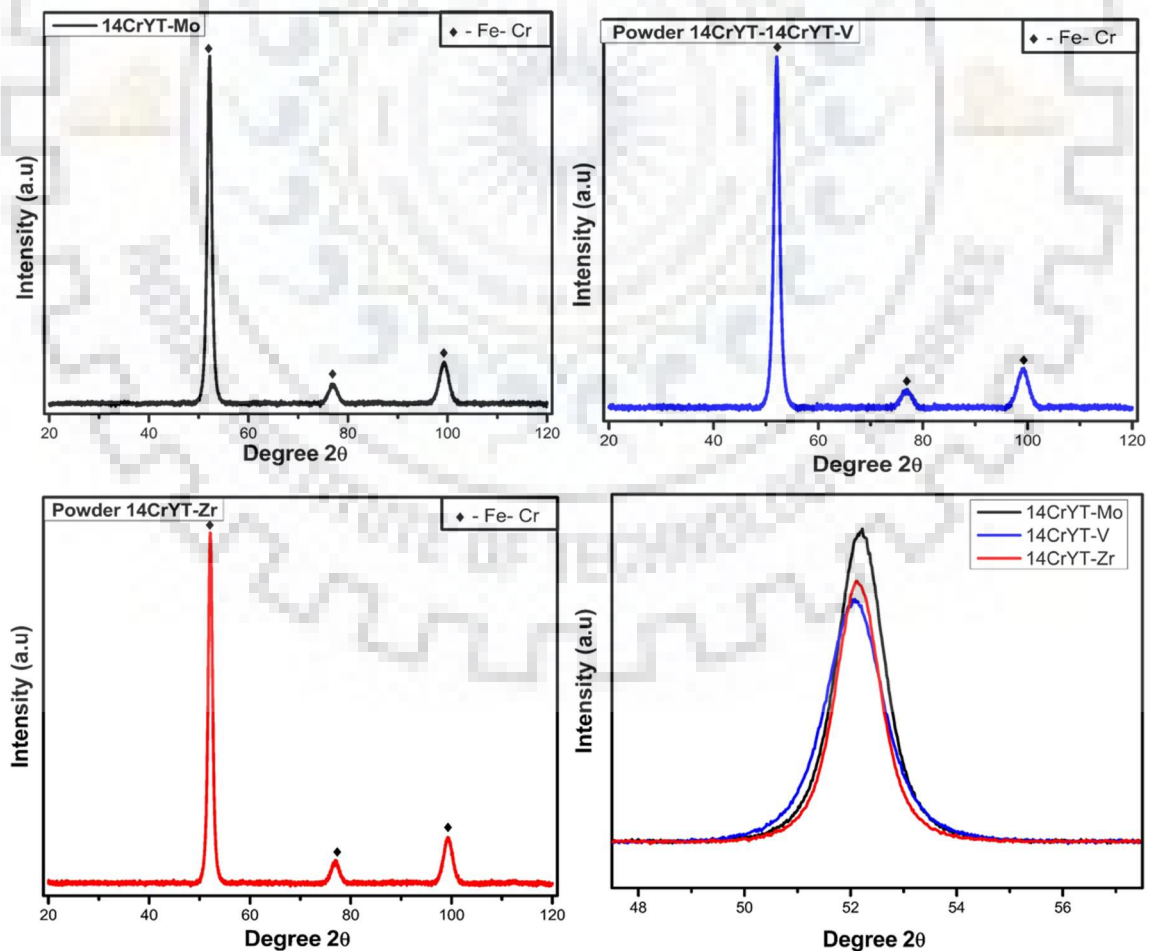
Fig. 25 XRD analysis of 25h milled ODS steel powders with different composition

4.2.2 TEM analysis

Fig. 26 shows the TEM images of mechanically alloyed powder which was milled for 25h. The dark image was used to analyse the crystallite size, the crystallite size was varying from 5nm-30nm for the as-milled samples. The average size was found to be 13.41nm (250 particles were studied to analyse the average size). This size was similar to the size achieved by V. M. S. Muthaiah, et.al [4] for Fe-11%Cr (~18nm) and Fe-14%Cr (~17nm) which was mechanically alloyed for 25h. The size of the crystalite was also analysed by XRD peaks by using Scherrer formula (Eq. 1), broaderning effect was eleminating peak by annealing the powder to 1100°C for 1h. The crystalite size measured from XRD analysis was 12.03nm which is corelating with the TEM results.
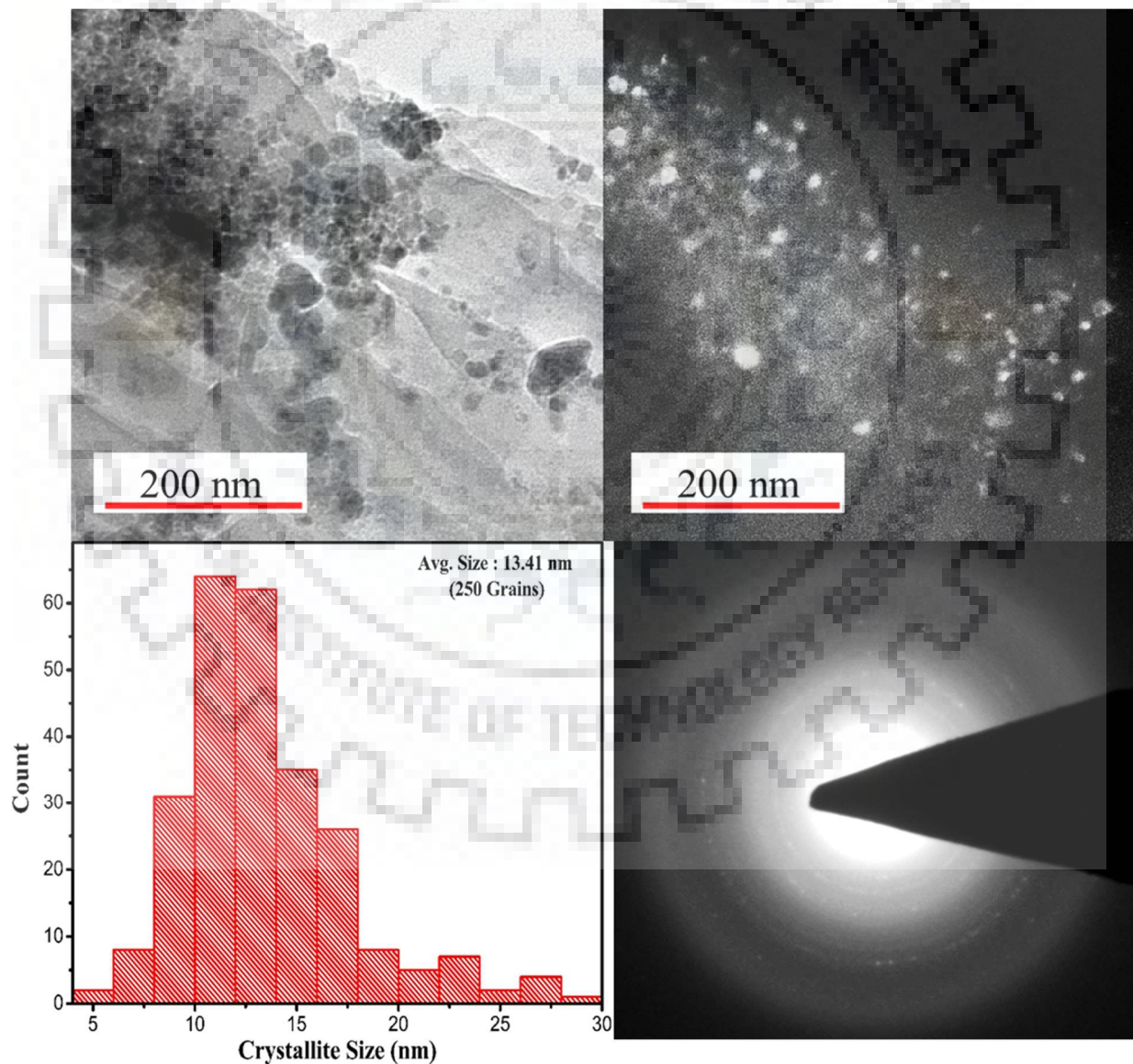
Fig. 26 TEM images of powders mechanically alloyed for 25h a)Bright Field b)Dark Field c)Histogram chart for crystallite size d) SAED pattern

4.3 Compacting and Sintering
4.3.1 SPS profile

The profile of the SPS process (**Fig. 27)** shows the displacement of the anvil, which can be used to correlate with the densification of the sample. The sample was sintered at the rate of 100°/min to required temperature and maintained at that temperature for 5mins. When electrically conductive metal materials are consolidated, non-thermal current effects may play a large role in the densification process, through enhanced (1) mass transport due to electro-migration, which arises from momentum transfer by conduction electrons scattering from the activated metal ions in the solid and pushing these ions in the direction of the electron flow; (2) point defect generation, and (3) defect mobility. The displacement of the anvil is more for the samples which at sintered at higher temperature, this shows that the porosity of the sample is getting filled up due to high pressure and diffusion in elevated temperature.
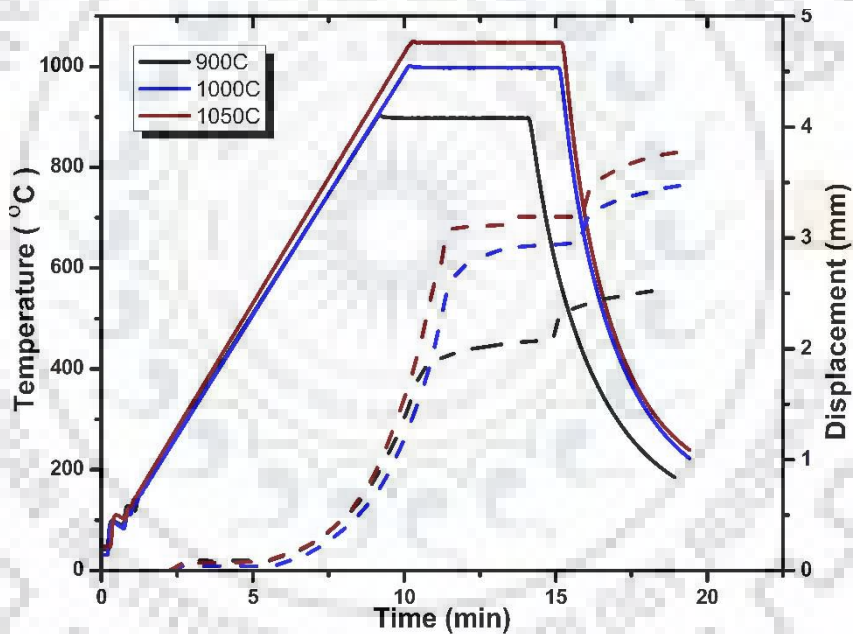
Fig. 27 SPS Profile

Fig. 28 shows the density of the samples prepared by SPS process in different temperatures. The density was noted to increase with sintering temperature. The relative density of 900°C & 1000°C sintered sample was found to be 80-82% & 95-96%. There was a huge density difference of ~ 14%-15% between the samples sintered at 900°C & 1000°, this is correlating with the large difference in the movement of the anvil which can be observed from **Fig. 27**. The maximum relative density was found to be 97.5% relative density for sample with V addition and sintered at 1050°C.
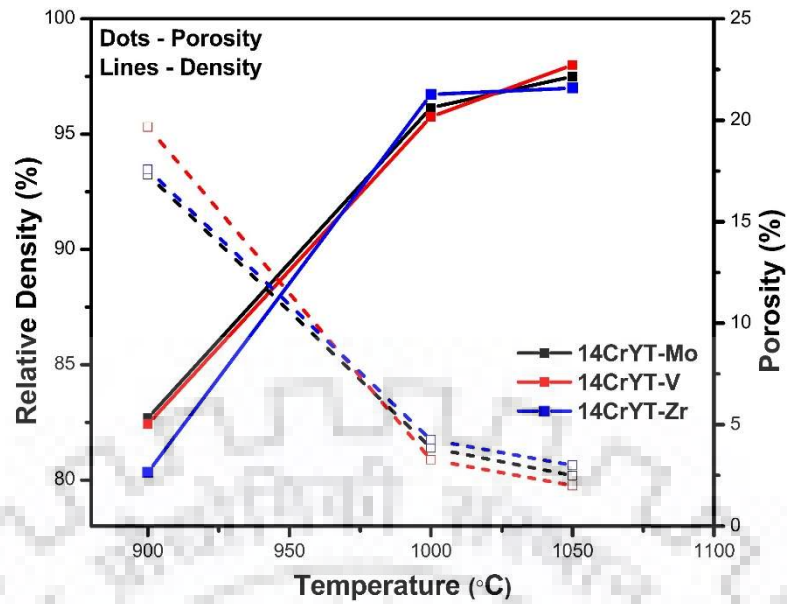
Fig. 28 Density of the sintered sample

4.3.2 XRD analysis

Fig. 29 show the XRD analysis carried out in the sintered samples, it can be note that the major peak intensity of Fe-Cr is getting less and new peak start to emerge with increase in the sintering temperature. The XRD analysis of this new peak shows that this peak is due to the formation of Fe-Cr-C phase.
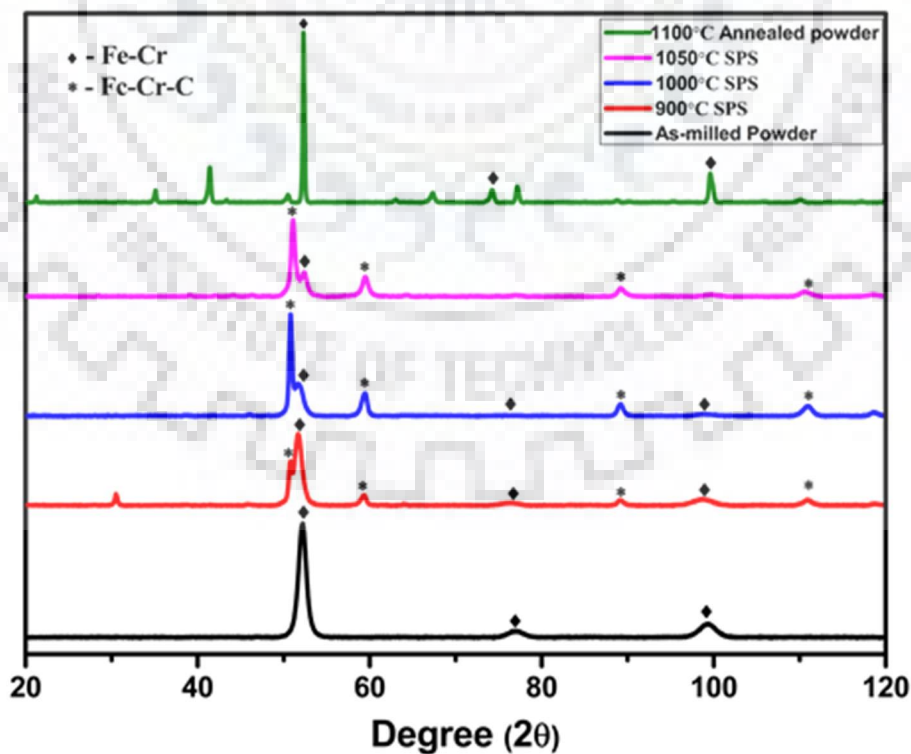
Fig. 29 XRD pattern of SPSed samples -With Carbon diffusion from the graphite protective layer

To check whether the diffusion of carbon is from any impurities present in the milled powders, annealing of the powders was done by holding the milled powders at 1100°C for 1h. The XRD pattern of this annealed powder does not shows any presence of Fe-Cr-C phase as shown in **Fig. 29**. Emergence of these new peaks was due to the diffusion of carbon atom in the sample when sintering at higher temperature, carbon from the graphite layer which was used to protect the sample from sticking, diffuses to forms a Fe-Cr-C phase. Similar kind of effect was reported by Xavier [63] (**Fig. 30**), in which it is was found that carbon has more diffusion capability than comparing to Ti, O, Y .
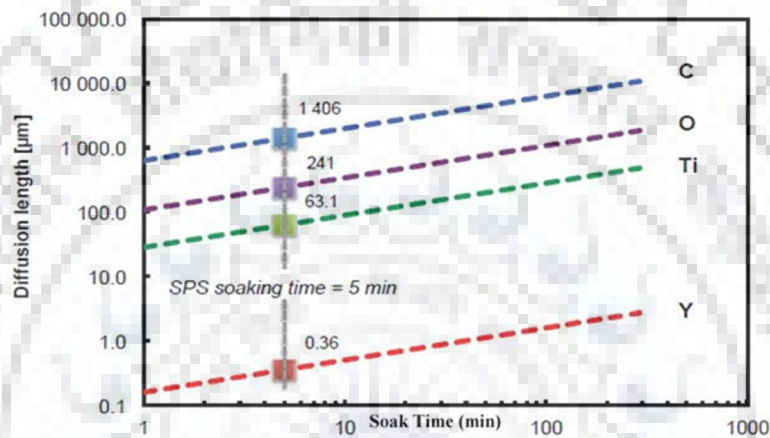
Fig. 30 Diffusion of various elements [63]

Xavier et al.[63], also found the depth of presentation of carbon though the sample, which was about 1600μm after which it was negligible as shown in **Fig. 31** . This also shows the variation in hardness of the samples will be there due to variation in carbon content along the depth. Therefore 0.5mm was removed from both the sides of the sample to avoid the presence of carbon content in the surface.
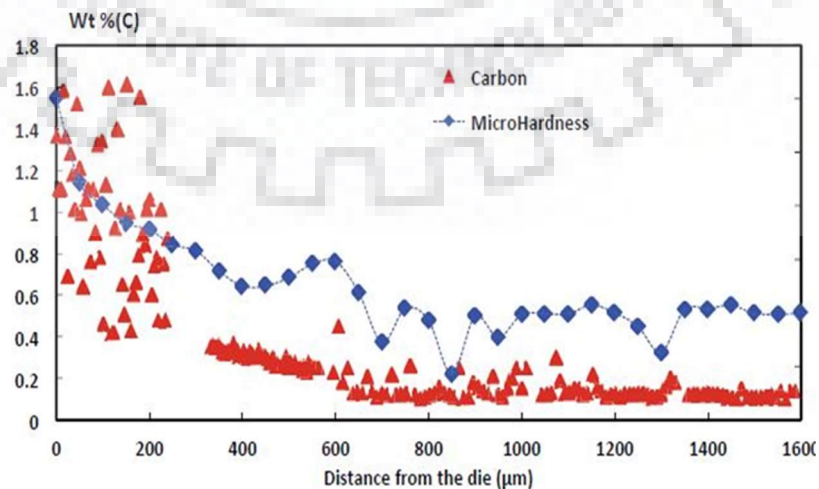
Fig. 31 Carbon concentration Vs Depth of penetration [63]
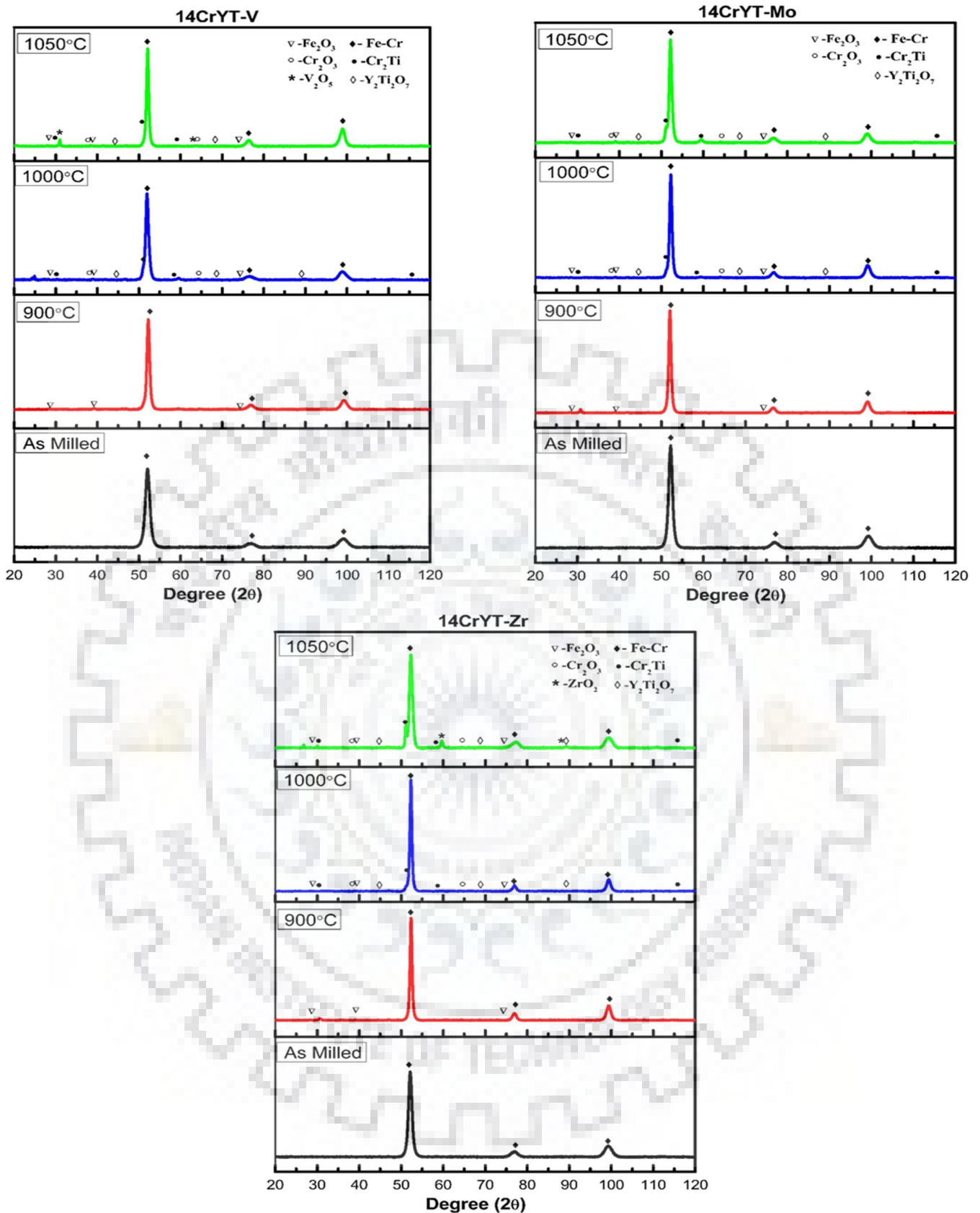
Fig. 32 XRD pattern for SPSed samples - After removing carbon diffused layers

The XRD was taken for the carbon layer removed sample and it doesn't show any presence of Fe-Cr-C phase at elevated temperature. **Fig. 32** shows the formation oxides and intermetallic phases emerges while sintering at higher temperatures, similar complex oxide like of $Y_2Ti_2O_7$ was reported by many researchers [64][65].

4.3.3 Optical microscopy

Fig. 33 shows the microstructure obtained by optical microscopy for the samples sintered at various temperatures. The microstructure of 900°C sintered sample shows the high porosity coincides with the results of SPS displacement and density. The porosity reduction can be seen as the sintering temperature increases due to bonding occurring by diffusion at higher temperature. The microstructure of 1050°C shows the bimodal microstructure, similar to the microstructure obtained by H.Zhang, et.al. [65], which improves the hardness of the material as well as retaining the toughness of the material to some extent. The dark spots are not visible in the samples sintered at 1050 °C shows that the porosity level is negligible.
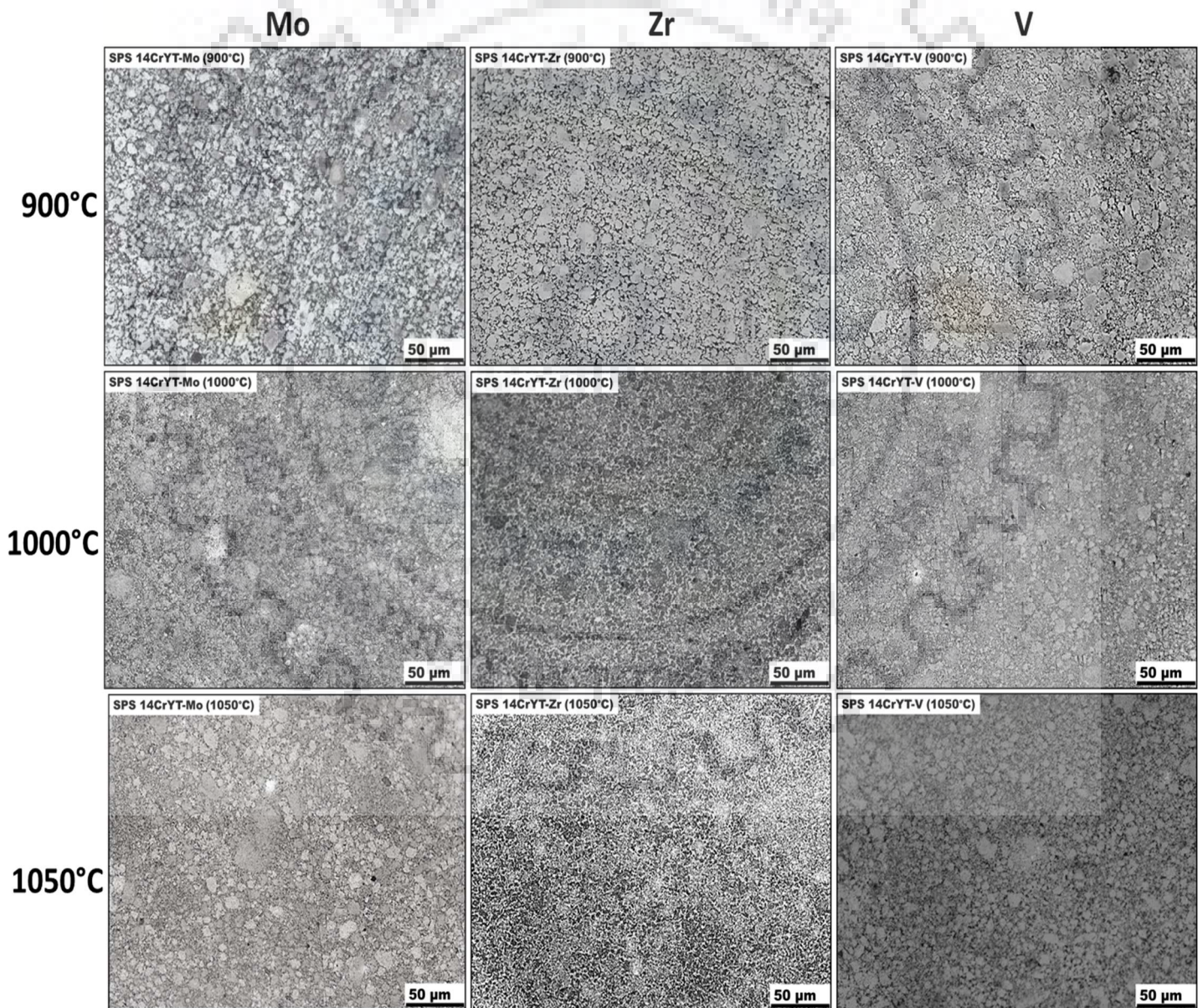
Fig. 33 Microstructure of SPSed samples taken by optical microscopy

4.3.4 SEM analysis

     Fig. 34 shows SEM analysis carried out on the sintered sample in both secondary electron and backscatter electron mode. The porosity for the sample sintered at 900°C is higher, which can be seen by the numerous free-standing particles which are present without showing any neck-formation with the neighbouring particles. Porosity reduces drastically when sintering temperature was increased to 1000°C. This is because, diffusion of atoms increases along the necking area at higher temperature which creates more bonding within the particle and thus reduces the porosity.
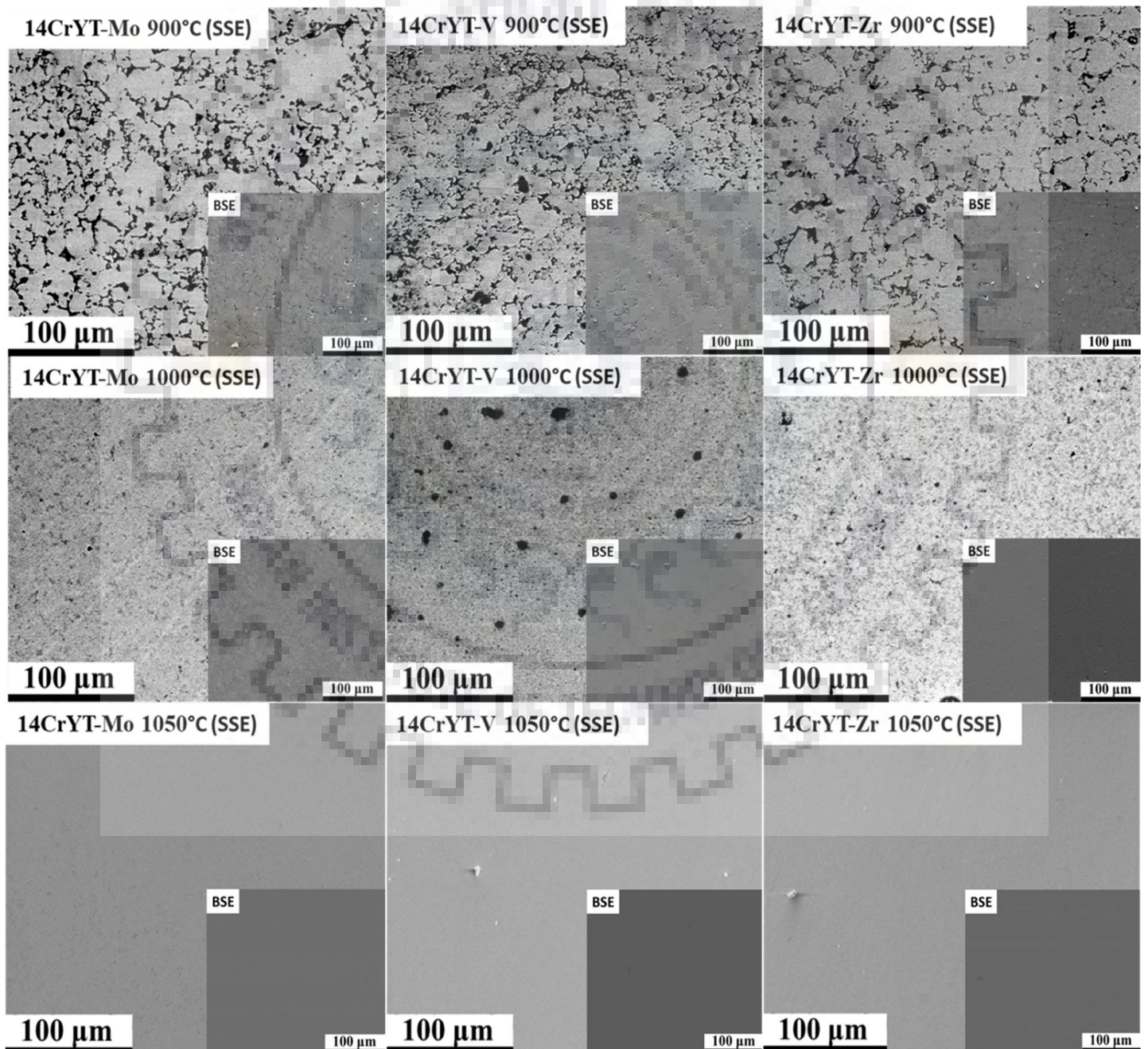
Fig. 34 SEM images of sintered sample

4.3.5 TEM analysis

TEM analysis of sample sintered at 1050°C is shown in **Fig. 35,** it can be seen that the size of the grains is in bimodal microstructure, similar to the microstructure proposed by optical microscopic analysis. SAED pattern also conforms the presence of intermetallic phases like Cr_2Ti, $Fe_{17}Y_2$ and oxides like $Y_2Ti_2O_7$, Cr_2O_3, TiO_2; correlating with the results obtained through XRD analysis. Neither SAED pattern nor the XRD pattern shows the presence of elementary constituents separately, which confirms the formation of single solid solution of Fe-Cr and partial amount of intermetallic which was mentioned before. The grin size was within the range of 200nm after sintering the sample at 1050°C. This grain growth stability may be achieved due to the formation of oxide particles which hinders the growth of grains in higher temperature and thus gives thermal stability while sintering the sample.
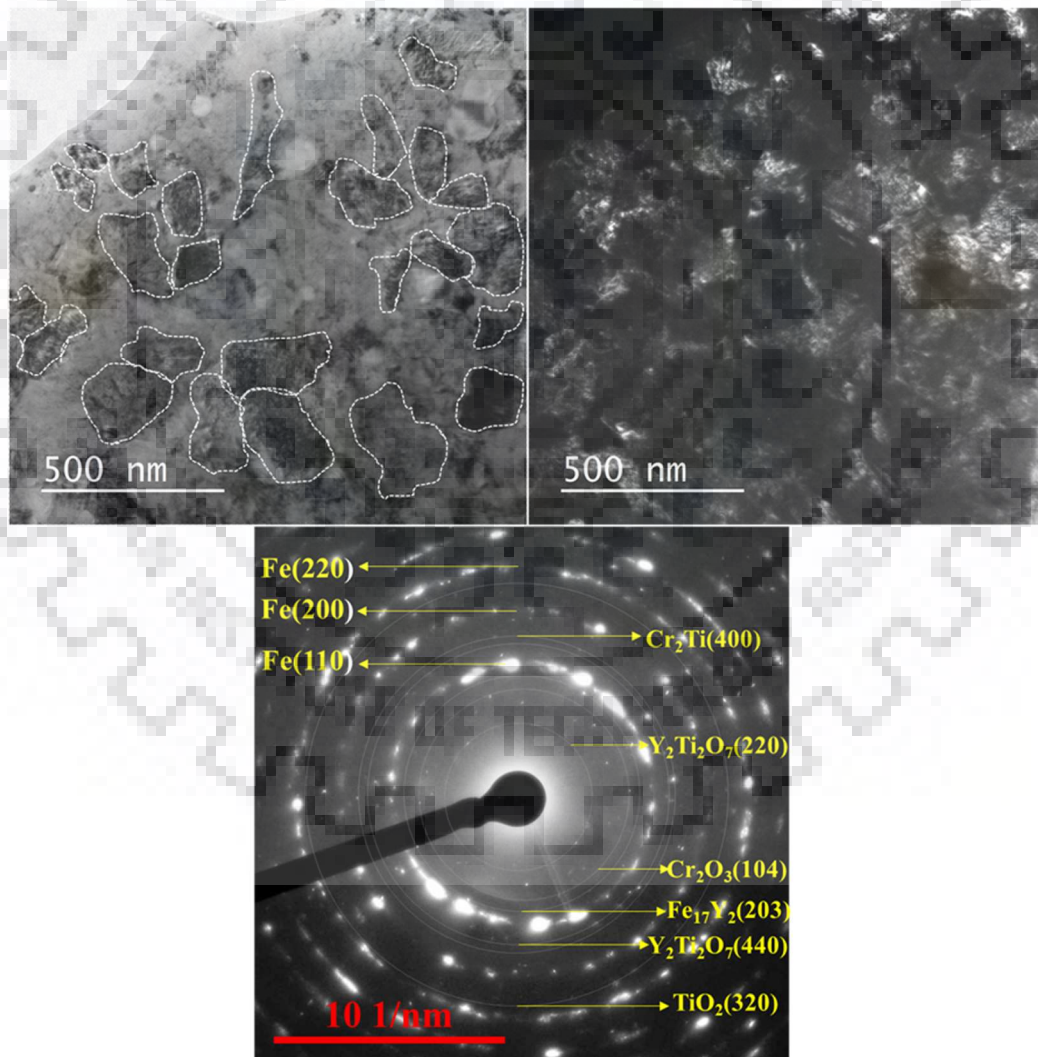
Fig. 35 TEM images of sample sintered at 1050 °C
a)Bright field b)Dark field c)corresponding SAED pattern
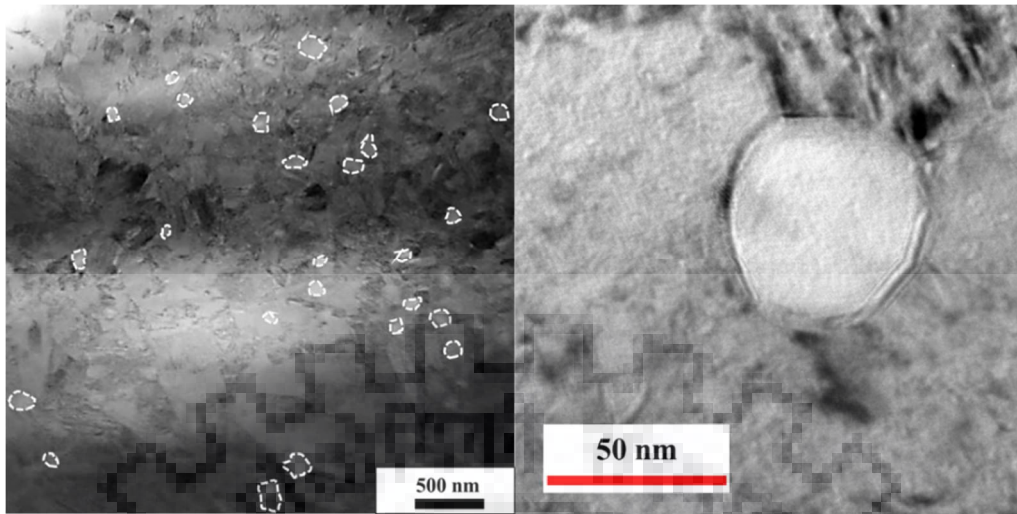
Fig. 36 TEM images showing oxide particles dispersed in the ferritic matrix sample sintered at 1050 ℃

Fig. 36 shows the presence of oxide particles in the ferritic matric, it can be observed that the oxide particles are in the range of 30-40nm. Since the size of oxides is very small, it improves the thermal stability of the samples without losing the properties such as creep, structural strength. **Fig. 37** shows EDS mapping of oxides present in the ferritic matrix. It can be noted from yttrium element mapping that there are some small yttrium clusters which shows the presence of Y-Ti-O. The presence of other oxides like Cr_2O_3, TiO_2, Ti-Cr-O can also be found from the EDS mapping.
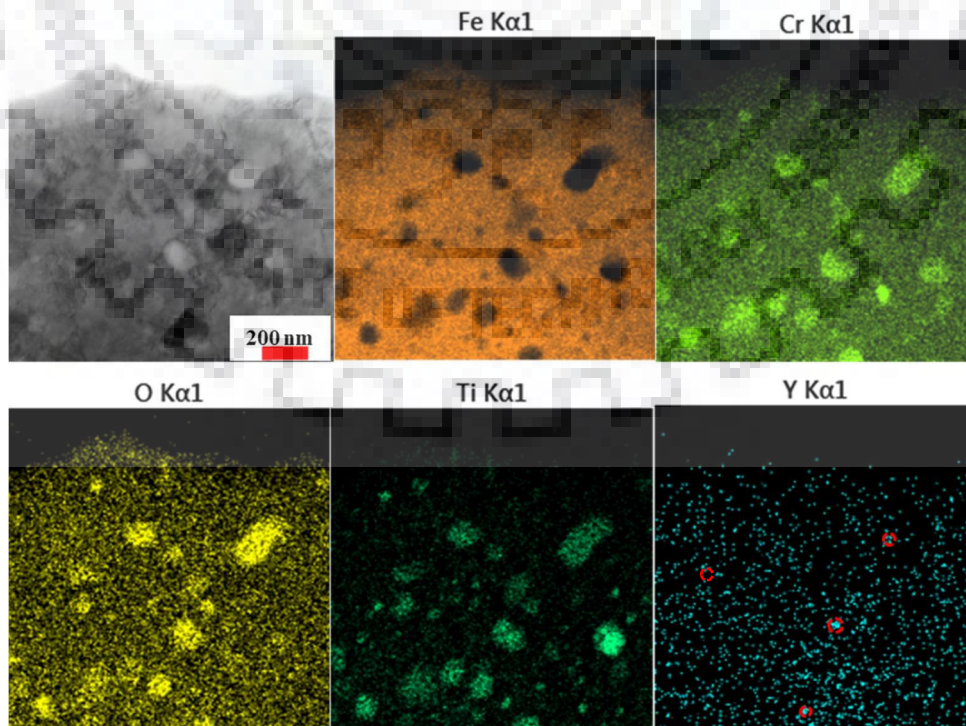
Fig. 37 STEM image and EDS mapping of SPSed samples at 1050 ℃

4.4 Mechanical Properties
4.4.1 Nanoindentation Test

Fig. 38 (a) shows the nanoindentation profile done on the samples which was sintered at 1050°C in SPS. The profile of the nanoindentation is used to find out the hardness and elastic modulus of the material. The displacement of the indenter through the sample is inversely proportional to the hardness of the material. The hardness of the sample sintered at 900°C is low due to improper bonding between the particles, but hardness increases rapidly for all the compositions which was sintered at 1000°C, this is due to the increase in density of the sample as well as due to formation of intermetallic and oxides while sintering. compare to other composition 14CrYT-V shows good hardness property.
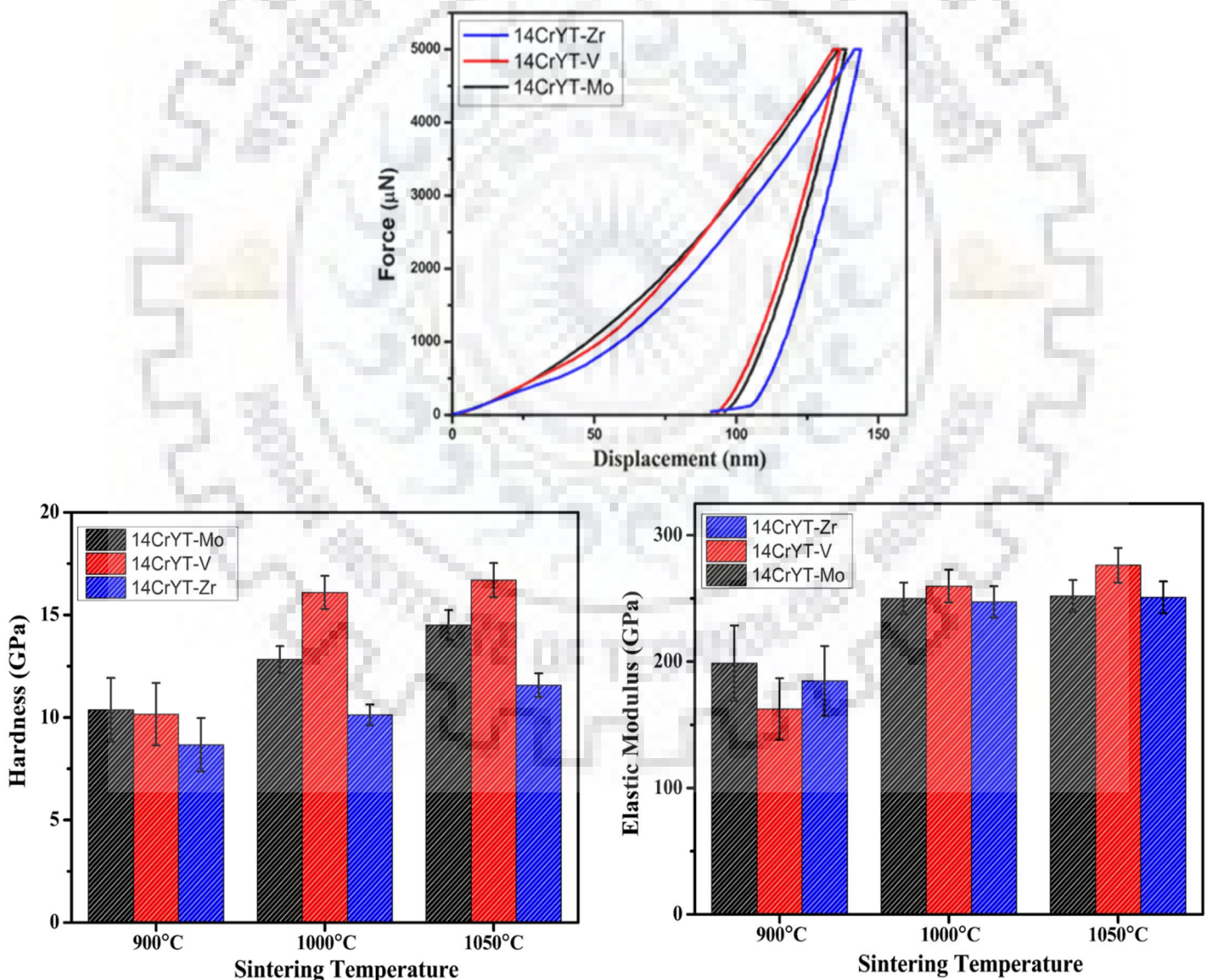
Fig. 38 Nanoindentation
a) indentation Profile on 1050C SPSed samples b)Hardness c)Elastic Modulus

35

The variation in hardness pattern is repeated similarly for the samples sintered at 1050°C also, for samples sintered at 1050°C, 14CrYT-V is showing a high hardness of about ~13% more that 14CrYT-Mo sample and ~30% more than 14CrYT-Zr sample. This might be due to formation of V_2O_5 in 14CrYT and also due to the high density achieved by this composition. Since Zr has high affinity towards oxygen it could have hindered the formation of complex oxides which could have increase the strength of his composition.

The formation of this complex oxides can increase the strength as well as does not hinder the ductile nature of the material due to its coherence with matrix. Formation of intermetallic compounds also plays a major role in grain stabilisation and also increase the hardness and elastic modulus of the alloy. The elastic modulus of the all the alloys does not show any major variation as it showed in hardness. 14CrYT-V was giving high elastic modulus of about ~8% more that 14CrYT-Mo sample and ~9% more than 14CrYT-Zr sample.

4.4.2 Compression Test

Compression test on the samples sintered at 1050°C was carried out and stress-strain graph is drawn (**Fig. 39**) from the load and displacement of anvil data obtained from the compression test machine.
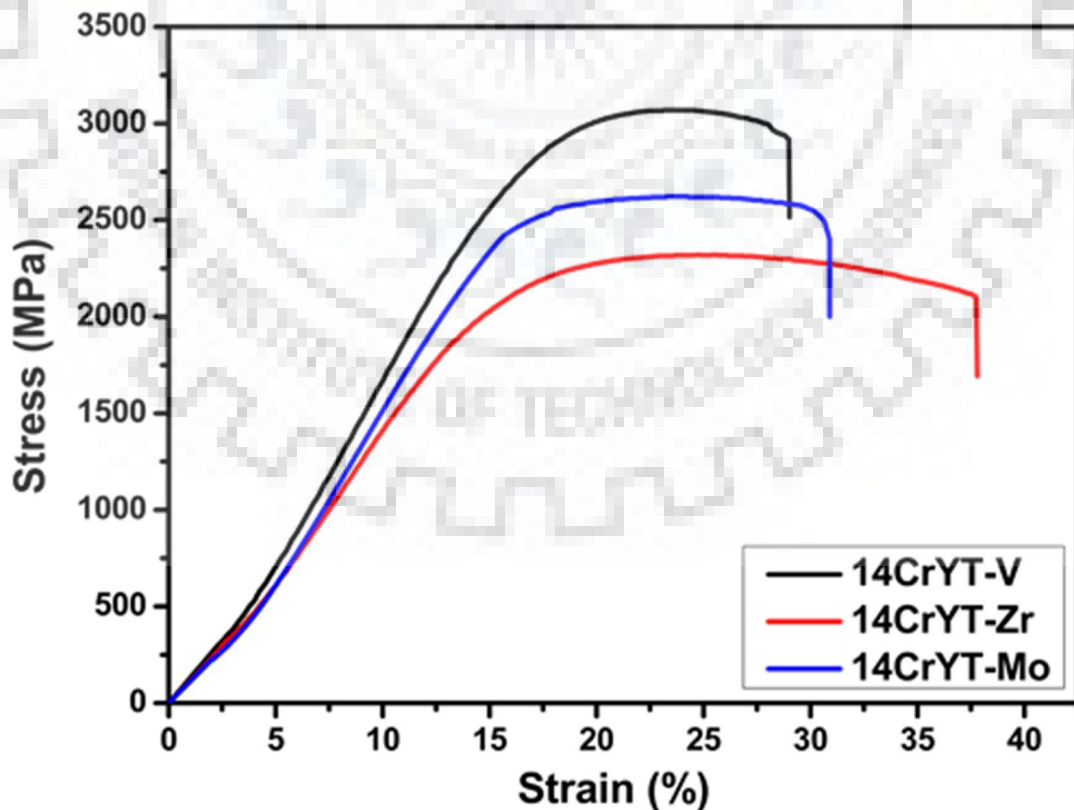
Fig. 39 Compression test on samples SPSed at 1050°C

Table 2 Properties of Samples sintered at 1050 ℃

Alloys	Hardness (GPa)	Elastic Modulus (GPa)	Compression Stress (MPa)	Strain at fracture point (%)
14CrYT- Mo	14.51113	251.96768	2621.875	30.9
14CrYT- V	16.6975	276.17648	3068.75	29.025
14CrYT- Zr	11.57419	250.8779	2320	37.8

Only samples sintered at 1050°C was selected for compression test, this is because the density of these samples are near to the theoretical. Analysis of the XRD patterns (**Fig. 32**) and TEM analysis (**Fig. 35)** endorse the presence of intermetallic (Cr_2Ti, $Fe_{17}Y_2$), which are likely would have contributed for the increase in the strength to the Fe-Cr matrix due to precipitation strengthening mechanism. The alloy which contains V show the best result compare to the other compositions. This high strength is due to the presence of oxides like V_2O_5, $Y_2Ti_2O_7$ and intermetallic present in the material. The strain at which the sample fails was low for the 14CrYT-V samples, because with increase in hardness of the materials the ductile nature of the material diminishes. The strain rate was lowering as the hardness of the sample is increased. The fracture happened due to the shear force applied on the sample on applying the compression load. The presence of the complex nano-sized oxide particles increases the strength and also due to their surface coherence with the matrix toughness of the sample is retained.

4.4.3 Wear Test

The difference in the coefficient of friction (COF) during dry sliding wear as a function of time for the SPSed 14CrYT-Mo, 14CrYT-V and 14CrYT-Zr samples (sintered at 1050°C) is as shown in **Fig. 40**. Generally, the value of COF increases to a peak value during the initial running-in-period and thereafter attained a steady state and remain constant. It can be seen that the COF of the samples decreases with increase in load this type of variation was also reported by S.Gupta, et.al. [66]. The COF of 14CrYT-Zr was low when applied with the load of 10N and 20N, this might be due to the formation of ZrO_2 which has the tendency to lower the coefficient of friction significantly [67]. The COF of 14CrYT-Zr was not low in case 5N load, because the sample might experience less wear out of ZrO_2 particle debris due to low load condition. The COF of 14CrYT-Mo and 14CrYT-V almost is same in all cases, ~0.84 for 10N load and ~0.82 for 20N load.
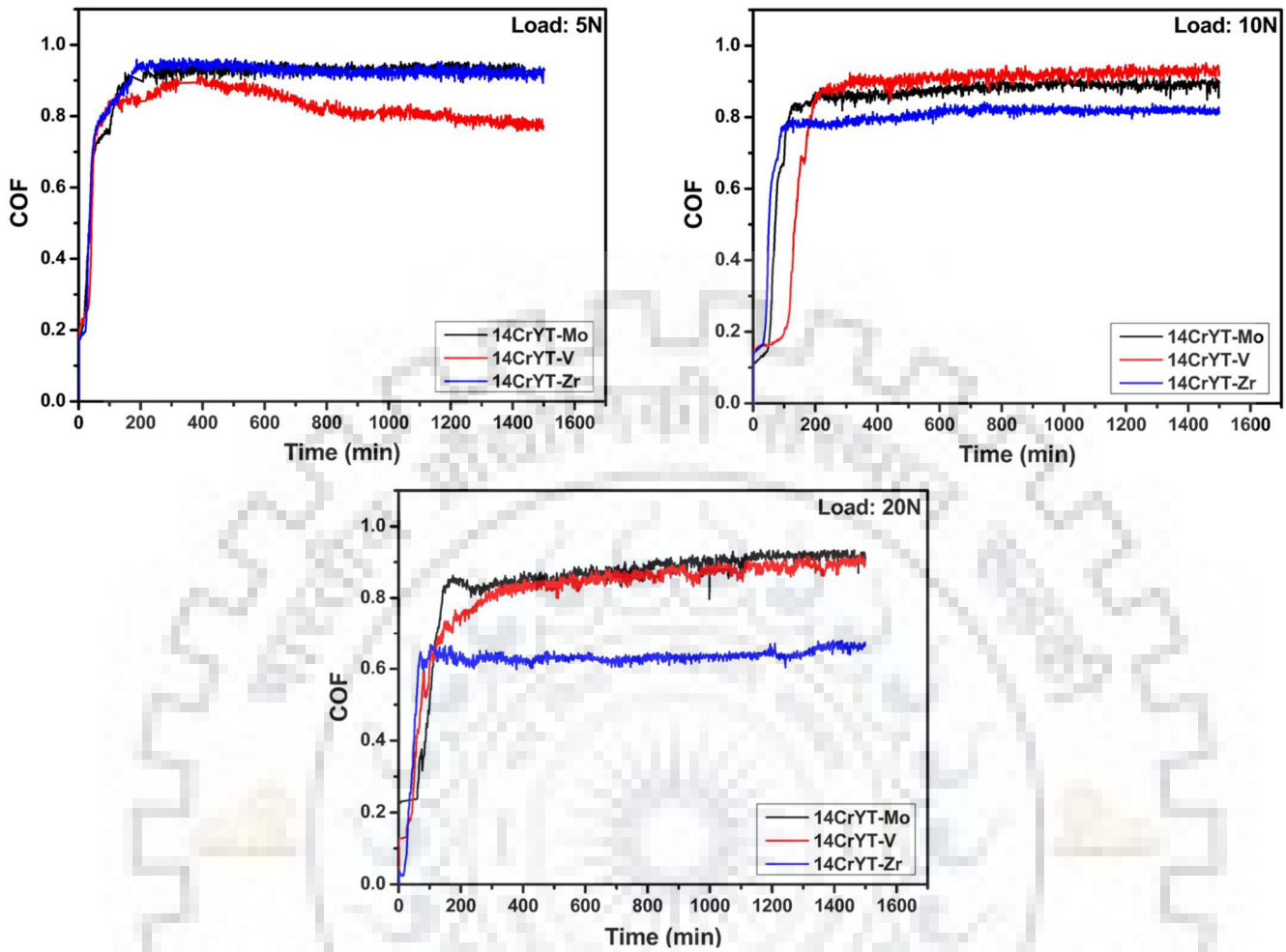
Fig. 40 Coefficient of friction for the samples sintered at 1050℃ tested at different loads

Wear volume is directly proportional to the hardness of the material, it can be clearly seen from the **Fig. 41**, that the wear depth was more for the samples which have less hardness. The surface profile of the wear track is taken with a scan speed of 0.05 mm/s so that the profile will not have any error. The waviness present in the surface profile is due to the wear debris present in the wear scar surface. It was observed that the wear depth increases with increase in applied load. As shown in **Fig. 42**, wear track was analysed by SEM to find the width of the wear track. It is clearly seen that the wear track increases with increase in the applied wear load.

The wear volume (V_d) is calculated by,

$$V_d = 2\pi r W D \tag{2}$$

Where, W is the width of the wear track measured from SEM image,

D is the depth of the wear track calculated by profilometer.
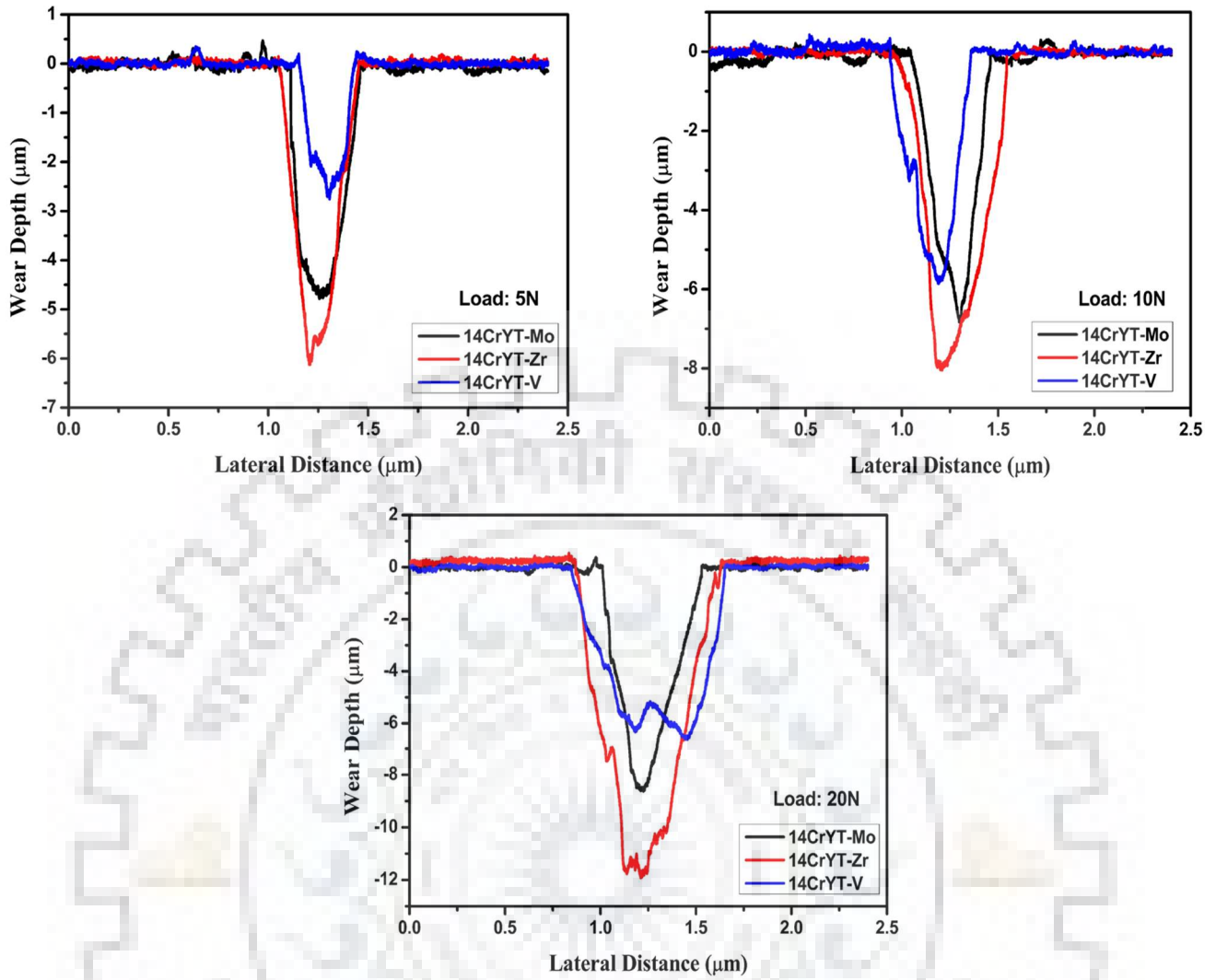
Fig. 41 Surface profile of wear track for different loads

With the help of the Eq. 2 and the value obtained from profilometer(wear depth) and SEM of wear track(wear width), wear volume is calculated. The wear volume was more in case of 14CRYT-Zr this is due to the abrasive nature of the ZrO_2 which can increase the wear rate of the sample by abrasive wear mechanism. **Fig. 43** shows the wear volume loss in all the samples sintered at 1050°C for different loads. The wear volume loss of 14CrYT-V is less compare to other compositions due to its high hardness than other samples.

Wear rate (WR) of the sample is found by the following formula

$$WR = \frac{V_d}{PS} \tag{3}$$

Where, V_d is the wear volume (mm^3)

P is the applied load (N)

S is the sliding distance (m)

39
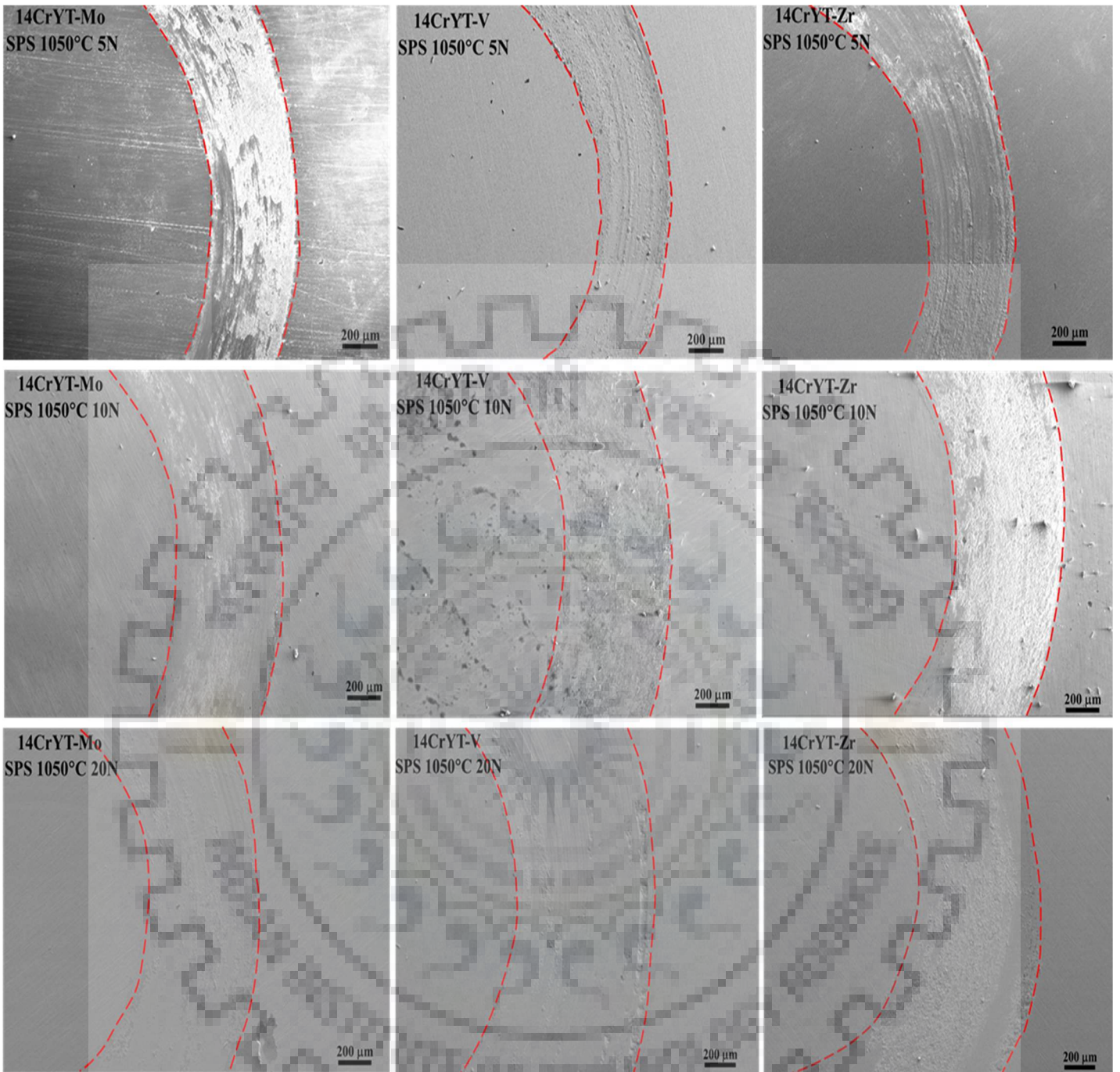
Fig. 42 SEM images of Wear track for different load conditions

Fig. 44 show the variation in wear rate with respect to different load condition. It can be seen that the wear rate of 14CrYT-Zr is more in all three conditions. This is due to the abrasive wear mechanism offered by the ZrO_2 particles present in the wear debris. It can also be noted that the wear rate decreases with increase in applied normal load. It can be observed that the COF of 14CrYT-Zr is low but wear volume is more similar results were noticed by S.K. Karak, et.al. [31].

40
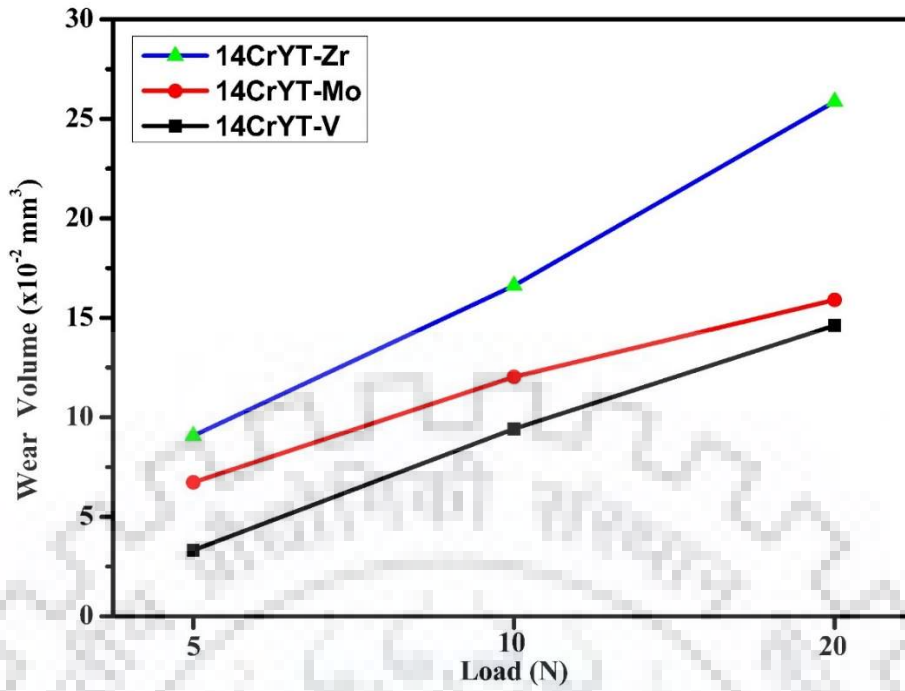
Fig. 43 Wear Volume at different loads

This decrease in wear rate might occur due to strain hardening of the material near to the wear out surface which can offer resistance to wear further. But this layers which offers resistance has limit after which these layers will cut off suddenly which can increase the wear volume as it is observed in as it is observed in **Fig. 43.** Presence of complex oxide particles can offer good wear resistance, similar observation was noticed by Karak, et.al. [31].
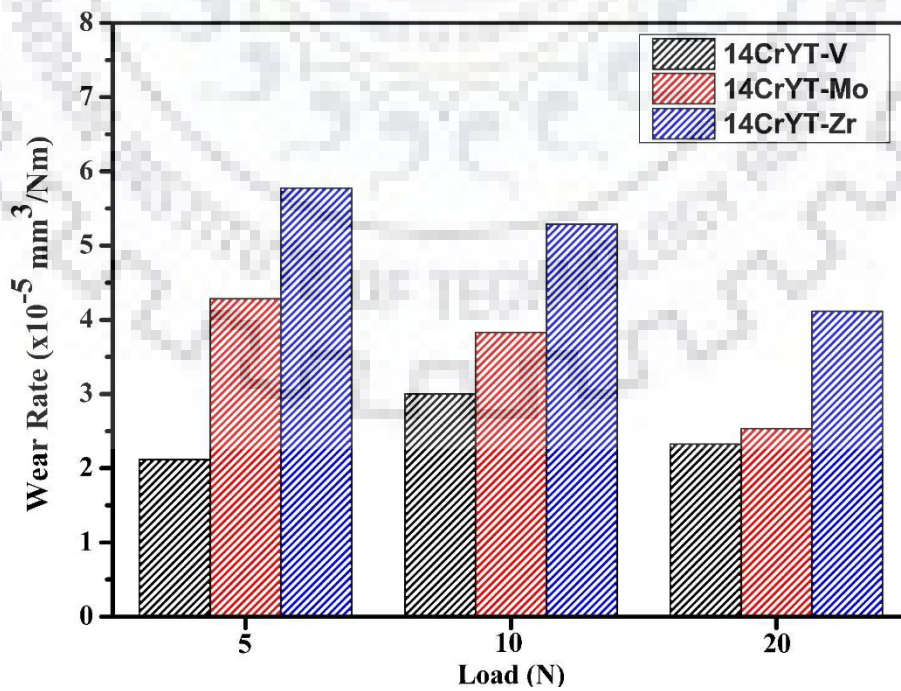
Fig. 44 Wear rate at different loads

41

CHAPTER 5   CONCLUSION

5.1 Conclusions

Fe-Cr based ODS alloys for high strength fusion structural applications were developed by 25h mechanical alloying of commercially available pure elemental powders. Milled powders were then sintered using SPS process at various temperatures (900°C, 1000°C, 1050°C). Mechanical properties and microstructural characteristics were investigated in detail. The following findings may be summarized from the results and analysis of the present study.

1) As-milled sample showed a single phase solid solution developed after 25h of milling, complete dissolution of all the other elements like Cr, Ti, Mo, Zr, V was achieved. Crystallite size of the milled powder was ~13.41nm and the grain size was confirmed by TEM analysis.

2) Maximum density was archived for the samples sintered at 1050°C, the relative density achieved at 1050°C is ~97.5%.

3) Optical and SEM analysis of microstructure showed that the level of porosity decreased with increase in sintering temperature. The microstructure formed after sintering was found to be bimodal in nature.

4) TEM and EDS mapping confirms the presence of complex oxides like Y-Ti-O, Ti-Cr-O with other oxides like TiO and Cr_2O_3, with particle size ranging from 30-40nm.

5) Nanoindentation test showed that the hardness and elastic modulus were more for the sample sintered at 1050°C. Hardness value for 14CrYT-V SPSed sample was found to be 16.7 GPa which was higher than other compositions.

6) The compression strength and wear resistance of 14CrYT-V SPSed sample were more for the sample sintered at 1050°C, and these correlated well with the hardness and density of the corresponding sample.

5.2 Future scopes

➢ Properties such as fracture toughness, creep resistance should be studied.

➢ Corrosion resistance of the samples sintered at various temperature need to be analysed.

➢ The concentration of the oxide particles need to be analyzed by atom probe topography.

➢ EBSD analysis should be carried out to get more details on the microstructure such as misorientation of grains boundaries.

Reference

[1] **E. A. Marquis, J. M. Hyde, D. W. Saxey, S. Lozano-perez, V. De Castro, D. Hudson, C. A. Williams, S. Humphry-baker, and G. D. W. Smith**, "Nuclear reactor materials at the atomic scale," *Mater. Today*, vol. 12, no. 11, pp. 30–37, 2009.

[2] **K. L. Murty and I. Charit**, "Structural materials for Gen-IV nuclear reactors: Challenges and opportunities," *J. Nucl. Mater.*, vol. 383, no. 1–2, pp. 189–195, 2008.

[3] **R. J. Kenny and M. W. Leff**, "Dispersion Strengthened Ferritic Alloy for use in Liquid-Metal Fast Breeder Reactors (LMFBRS)," *U.S. Pat. 4,075,010 A*, pp. 1–6, 1978.

[4] **V. M. S. Muthaiah, L. H. Babu, C. C. Koch, and S. Mula**, "Feasibility of formation of nanocrystalline Fe-Cr-Y alloys: Mechanical properties and thermal stability," *Mater. Charact.*, vol. 114, pp. 43–53, 2016.

[5] **P. Shahbeigi Roodposhti, M. Saber, C. Koch, R. Scattergood, and S. Shahbazmohamadi**, "Effect of oxygen content on thermal stability of grain size for nanocrystalline Fe10Cr and Fe14Cr4Hf alloy powders," *J. Alloys Compd.*, vol. 720, pp. 510–520, 2017.

[6] **S. Yamashita, K. Oka, S. Ohnuki, N. Akasaka, and S. Ukai**, "Phase stability of oxide dispersion-strengthened ferritic steels in neutron irradiation," *J. Nucl. Mater.*, vol. 307–311, no. 1 SUPPL., pp. 283–288, 2002.

[7] **W. Z. Xu, L. L. Li, M. Saber, C. C. Koch, Y. T. Zhu, and R. O. Scattergood**, "Nano ZrO2particles in nanocrystalline Fe-14Cr-1.5Zr alloy powders," *J. Nucl. Mater.*, vol. 452, no. 1–3, pp. 434–439, 2014.

[8] **X. M. Bai, A. F. Voter, R. G. Hoagland, M. Nastasi, and B. P. Uberuaga**, "Efficient annealing of radiation damage near grain boundaries via interstitial emission," *Science (80-.).*, vol. 327, no. 5973, pp. 1631–1634, 2010.

[9] **D. Chen, J. Wang, T. Chen, and L. Shao**, "Defect annihilation at grain boundaries in alpha-Fe," *Sci. Rep.*, vol. 3, no. 13, pp. 1–5, 2013.

[10] **S. Ukai, T. Kaito, S. Ohtsuka, T. Narita, and M. Fujiwara**, "Production and Properties of Nano-scale Oxide Dispersion Strengthened (ODS) 9Cr Martensitic Steel Claddings,"

ISIJ Int., vol. 43, no. 12, pp. 2038–2045, 2003.

[11] **C. Cayron, E. Rath, I. Chu, and S. Launois**, "Microstructural evolution of Y2O3and MgAl2O4ODS EUROFER steels during their elaboration by mechanical milling and hot isostatic pressing," *J. Nucl. Mater.*, vol. 335, no. 1, pp. 83–102, 2004.

[12] **S. Ukai, H. Okada, M. Inoue, T. Nishida, M. Fujiwara, S. Nomura, S. Shikakura, and K. Asabe**, "Alloying design of oxide dispersion for long life FBRs core materials strengthened ferritic steel," *J. Nucl. Mater.*, vol. 204, no. 6, pp. 5–73, 1993.

[13] **S. Ohtsuka, S. Ukai, M. Fujiwara, T. Kaito, and T. Narita**, "Nano-structure control in ODS martensitic steels by means of selecting titanium and oxygen contents," *J. Phys. Chem. Solids*, vol. 66, no. 2–4, pp. 571–575, 2005.

[14] **H. Sakasegawa, L. Chaffron, F. Legendre, M. Brocq, L. Boulanger, S. Poissonnet, Y. de Carlan, J. Bechade, T. Cozzika, and J. Malaplate**, "Evaluation of threshold stress of the MA957 ODS ferrtic alloy," *J. Nucl. Mater.*, vol. 386–388, no. C, pp. 511–514, 2009.

[15] **M. Zupan, M. Legros, B. R. Elliott, and K. J. Hemker**, "Microsample tensile testing of nanocrystalline metals and single-crystalline alloys," *Proc. TMS Fall Meet.*, pp. 1017–1027, 1999.

[16] **J. R. Weertman, D. Farkas, K. Hemker, H. Kung, M. Mayo, R. Mitra, and H. Van Swygenhoven**, "Structure and Mechanical Behavior of Bulk Nanocrystalline Materials," *MRS Bull.*, vol. 24, no. 2, pp. 44–53, Feb. 1999.

[17] **S. Z. Han, M. Goto, C. Lim, C. J. Kim, and S. Kim**, "Fatigue behavior of nano-grained copper prepared by ECAP," *J. Alloys Compd.*, vol. 434–435, no. SPEC. ISS., pp. 304–306, 2007.

[18] **E. Hosseini and M. Kazeminezhad**, "The effect of ECAP die shape on nano-structure of materials," *Comput. Mater. Sci.*, vol. 44, no. 3, pp. 962–967, 2009.

[19] **S. Bera, W. Lojkowsky, and I. Manna**, "Development of wear-resistant Cu-10Cr-3Ag electrical contacts with nano-Al2O3 dispersion by mechanical alloying and high pressure sintering," *Metall. Mater. Trans. A Phys. Metall. Mater. Sci.*, vol. 40, no. 13, pp. 3276–3283, 2009.

[20] **D. Roy, R. Mitra, T. Chudoba, Z. Witczak, W. Lojkowski, H. J. Fecht, and I. Manna**,

"Structure and mechanical properties of Al65Cu20Ti15-based amorphous/nanocrystalline alloys prepared by high-pressure sintering," *Mater. Sci. Eng. A*, vol. 497, no. 1–2, pp. 93–100, 2008.

[21] **S. S. Singh, D. Roy, R. Mitra, R. V. Subba Rao, R. K. Dayal, B. Raj, and I. Manna**, "Studies on laser sintering of mechanically alloyed Al50Ti40Si10composite," *Mater. Sci. Eng. A*, vol. 501, no. 1–2, pp. 242–247, 2009.

[22] **Q. X. Sun, T. Zhang, X. P. Wang, Q. F. Fang, T. Hao, and C. S. Liu**, "Microstructure and mechanical properties of oxide dispersion strengthened ferritic steel prepared by a novel route," *J. Nucl. Mater.*, vol. 424, no. 1–3, pp. 279–284, 2012.

[23] **Q. X. Sun, Y. Zhou, Q. F. Fang, R. Gao, T. Zhang, and X. P. Wang**, "Development of 9Cr-ODS ferritic-martensitic steel prepared by chemical reduction and mechanical milling," *J. Alloys Compd.*, vol. 598, no. 3, pp. 243–247, 2014.

[24] **Y. P. Xia, X. P. Wang, Z. Zhuang, Q. X. Sun, T. Zhang, Q. F. Fang, T. Hao, and C. S. Liu**, "Microstructure and oxidation properties of 16Cr-5Al-ODS steel prepared by sol-gel and spark plasma sintering methods," *J. Nucl. Mater.*, vol. 432, no. 1–3, pp. 198–204, 2013.

[25] **R. Gao, T. Zhang, X. P. Wang, Q. F. Fang, and C. S. Liu**, "Effect of zirconium addition on the microstructure and mechanical properties of ODS ferritic steels containing aluminum," *J. Nucl. Mater.*, vol. 444, no. 1–3, pp. 462–468, 2014.

[26] **P. Miao, G. R. Odette, J. Gould, J. Bernath, R. Miller, M. Alinger, and C. Zanis**, "The microstructure and strength properties of MA957 nanostructured ferritic alloy joints produced by friction stir and electro-spark deposition welding," *J. Nucl. Mater.*, vol. 367–370 B, no. SPEC. ISS., pp. 1197–1202, 2007.

[27] **R. E. Schafrik and S. Walston**, "Challenges for High Temperature Materials in the New Millennium," *Superalloys 2008 11th Int. Symp. Superalloys*, pp. 3–9, 2008.

[28] **M. Nuthalapati**, "Alloys by Mechanical Alloying Followed by Conventional and Spark Plasma Sintering Metallurgical and Materials Engineering National Institute of Technology Rourkela Supervisor â€™ s Certificate," 2016.

[29] **P. Yvon and F. Carré**, "Structural materials challenges for advanced reactor systems," *J. Nucl. Mater.*, vol. 385, no. 2, pp. 217–222, 2009.

[30] **A. Alamo, V. Lambard, X. Averty, and M. H. Mathon**, "Assessment of ODS-14%Cr ferritic alloy for high temperature applications," *J. Nucl. Mater.*, vol. 329–333, no. 1–3 PART A, pp. 333–337, 2004.

[31] **S. K. Karak, C. S. Vishnu, Z. Witczak, W. Lojkowski, J. Dutta Majumdar, and I. Manna**, "Studies on wear behavior of nano-Y2O3dispersed ferritic steel developed by mechanical alloying and hot isostatic pressing," *Wear*, vol. 270, no. 1–2, pp. 5–11, 2010.

[32] **L. L. Snead, R. Yamada, K. Noda, Y. Katoh, S. J. Zinkle, W. S. Eatherly, and A. L. Qualls**, "In situ thermal conductivity measurement of ceramics in a fast neutron environment," *J. Nucl. Mater.*, vol. 283–287, no. PART I, pp. 545–550, 2000.

[33] **H. Nickel, F. Schubert, and H. Schuster**, "Evaluation of alloys for advanced high-temperature reactor systems," *Nucl. Eng. Des.*, vol. 78, no. 2, pp. 251–265, 1984.

[34] **I. Working, G. On, P. Of, A. S. Meeting, O. B. Y. The, I. Atomic, E. Agency, H. I. N. Cracow, I. Atomic, and E. Agency**, "High Temperature Metallic Materials For Gas-Cooled Reactors High Temperature Metallic Materials For Gas-Cooled Reactors," no. June 1988, pp. 20–23, 1989.

[35] **L. Dai, Y. Liu, and Z. Dong**, "Size and structure evolution of yttria in ODS ferritic alloy powder during mechanical milling and subsequent annealing," *Powder Technol.*, vol. 217, pp. 281–287, 2012.

[36] **R. J. Kenny and M. W. Leff**, "Dispersion Strengthened Ferritic Alloy For Use In Liquid-Metal Fast Breeder React Ors (LMFBRS)," *U.S. Pat. 4,075,010 A*, pp. 1–6, 1978.

[37] **R. L. Klueh and A. T. Nelson**, "Ferritic/martensitic steels for next-generation reactors," *J. Nucl. Mater.*, vol. 371, no. 1–3, pp. 37–52, 2007.

[38] **F. A. Garner, M. B. Toloczko, and B. H. Sencer**, "Comparison of swelling and irradiation creep behavior of fcc-austenitic and bcc-ferritic/martensitic alloys at high neutron exposure," *J. Nucl. Mater.*, vol. 276, no. 1, pp. 123–142, 2000.

[39] **S. Ukai, H. Okada, M. Inoue, T. Nishida, M. Fujiwara, S. Nomura, S. Shikakura, and K. Asabe**, "Alloying design of oxide dispersion for long life FBRs core materials strengthened ferritic steel," *J. Nucl. Mater.*, vol. 204, no. 6, pp. 5–73, 1993.

[40] **G. R. Odette, M. J. Alinger, and B. D. Wirth**, "Recent Developments in Irradiation-Resistant Steels," *Annu. Rev. Mater. Res.*, vol. 38, no. 1, pp. 471–503, 2008.

[41] **Z. Li, Z. Lu, R. Xie, C. Lu, Y. Shi, and C. Liu**, "Effects of Y 2 O 3 , La 2 O 3 and CeO 2 additions on microstructure and mechanical properties of 14Cr-ODS ferrite alloys produced by spark plasma sintering," *Fusion Eng. Des.*, vol. 121, pp. 159–166, 2017.

[42] **H. Sakasegawa, L. Chaffron, F. Legendre, L. Boulanger, T. Cozzika, M. Brocq, and Y. de Carlan**, "Correlation between chemical composition and size of very small oxide particles in the MA957 ODS ferritic alloy," *J. Nucl. Mater.*, vol. 384, no. 2, pp. 115–118, 2009.

[43] **S. Ukai and M. Fujiwara**, "Perspective of ODS alloys application in nuclear environments," *J. Nucl. Mater.*, vol. 307–311, no. 1 SUPPL., pp. 749–757, 2002.

[44] **C. Suryanarayana**, "Mechanical Alloying and Milling Mechanical Engineering," *Prog. Mater. Sci.*, vol. 46, pp. 1–184, 2001.

[45] **J. Eckert, K. Jost, and L. Schultz**, "Synthesis and properties of mechanically alloyed Y-Ni-B-C," *Mater. Lett.*, vol. 31, no. 3–6, pp. 329–333, 1997.

[46] **K. Okada, S. Kikuchi, T. Ban, and N. Otsuka**, "Difference of mechanochemical factors for Al2O3powders upon dry and wet grinding," *J. Mater. Sci. Lett.*, vol. 11, no. 12, pp. 862–864, 1992.

[47] **B. P. Dolgin, M. A. Vanek, T. McGory, and D. J. Ham**, "Mechanical alloying of Ni, CO, and Fe with Ti. Formation of an amorphous phase," *J. Non. Cryst. Solids*, vol. 87, no. 3, pp. 281–289, 1986.

[48] **J. S. Benjamin**, "Fundamentals of Mechanical Alloying," *Mater. Sci. Forum*, vol. 88–90, pp. 1–18, 1992.

[49] **D. Singh, C. Suryanarayana, L. Mertus, and R. H. Chen**, "Extended homogeneity range of intermetallic phases in mechanically alloyed Mg-Al alloys," *Intermetallics*, vol. 11, no. 4, pp. 373–376, 2003.

[50] **S. K. Pabi, J. Joardar, and B. S. Murty**, "Mechanism and Kinetics of alloying and nanostructure formation by mechanical methods," *Pinsa*, vol. 1, no. 1. pp. 1–30, 2001.

[51] **M. Yusoff and Z. Hussain**, "Effect of Sintering Parameters on Microstructure and Properties of Mechanically Alloyed Copper-Tungsten Carbide Composite," *Int. J. Mater. Mech. Manuf.*, vol. 1, no. 3, pp. 283–286, 2013.

[52] **S. Sōmiya**, *Handbook of advanced ceramics : materials, applications, processing, and properties*. .

[53] **C. Teodosio, A. C. García-Montero, M. Jara-Acevedo, L. Sánchez-Muñoz, I. Álvarez-Twose, R. Núñez, L. B. Schwartz, A. F. Walls, L. Escribano, and A. Orfao**, "Mast cells from different molecular and prognostic subtypes of systemic mastocytosis display distinct immunophenotypes," *J. Allergy Clin. Immunol.*, vol. 125, no. 3, 2010.

[54] **M. Tokita**, "Recent Progress of Spark Plasma Sintering (SPS) Method and Industrial use of Functionally Graded Materials (FGMs)," vol. 1, pp. 3–6, 2014.

[55] **K. Rajeswari, U. S. Hareesh, R. Subasri, D. Chakravarty, and R. Johnson**, "Comparative evaluation of spark plasma (SPS), microwave (MWS),two stage sintering (TSS) and conventional sintering (CRH) on the densification and micro structural evolution of fully stabilized zirconia ceramics," *Sci. Sinter.*, vol. 42, no. 3, pp. 259–267, 2010.

[56] **X. Li, Y. Ye, Y. Tang, and S. Qu**, "Effect of Pulsed Magnetic Field on Spark Plasma Sintering of Iron-Based Powders," *Mater. Trans.*, vol. 51, no. 7, pp. 1308–1312, 2010.

[57] **J. Schmidt, T. Weissgaerber, T. Schubert, and B. Kieback**, "Spark Plasma Sintering of Intermetallics and Metal Matrix Composites," pp. 93–98.

[58] **P. Figiel, M. Rozmus, and B. Smuk**, "Properties of alumina ceramics obtained by conventional and non-conventional methods for sintering ceramics," *J. Achiev. Mater. Manuf. Eng.*, vol. 48, no. 1, pp. 29–34, 2011.

[59] **J. R. Groza and A. Zavaliangos**, "Sintering activation by external electrical field," *Mater. Sci. Eng. A*, vol. 287, no. 2, pp. 171–177, 2000.

[60] **O. Guillon, J. Gonzalez-Julian, B. Dargatz, T. Kessel, G. Schierning, J. Räthel, and M. Herrmann**, "Field-assisted sintering technology/spark plasma sintering: Mechanisms, materials, and technology developments," *Adv. Eng. Mater.*, vol. 16, no. 7, pp. 830–849, 2014.

[61] **V. M. S. Muthaiah and S. Mula**, "Influence of Cr and Y Addition on Microstructure, Mechanical Properties, and Corrosion Resistance of SPSed Fe-Based Alloys," *Metall. Mater. Trans. A Phys. Metall. Mater. Sci.*, vol. 49, no. 3, pp. 990–1005, 2017.

[62] **B. D. Cullity and S. R. Stock**, *Elements of X-ray Diffraction*. Prentice Hall Upper Saddle

River, 2001.

[63] **M. De Lyon, X. Boulnat, A. Deschamps, and M. Perez**, "FAST high-temperature consolidation of Oxide-Dispersion Strengthened (ODS) steels : process, microstructure, precipitation, properties.," 2014.

[64] **S. K. . e Karak, J. D. . D. Majumdar, W. . Lojkowski, A. . Michalski, L. . Ciupinski, K. J. Kurzydłowski, I. . d Manna, K. J. . Kurzydowski, and I. . d Manna**, "Microstructure and mechanical properties of nano-Y 2O 3 dispersed ferritic steel synthesized by mechanical alloying and consolidated by pulse plasma sintering," *Philos. Mag.*, vol. 92, no. 5, pp. 516–534, 2012.

[65] **H. Zhang, Y. Huang, H. Ning, C. A. Williams, A. J. London, K. Dawson, Z. Hong, M. J. Gorley, C. R. M. Grovenor, G. J. Tatlock, S. G. Roberts, M. J. Reece, H. Yan, and P. S. Grant**, "Processing and microstructure characterisation of oxide dispersion strengthened Fe–14Cr–0.4Ti–0.25Y2O3 ferritic steels fabricated by spark plasma sintering," *J. Nucl. Mater.*, vol. 464, pp. 61–68, 2015.

[66] **S. Gupta, S. K. Sharma, B. V. M. Kumar, and Y.-W. Kim**, "Tribological characteristics of SiC ceramics sintered with a small amount of yttria," *Ceram. Int.*, vol. 41, no. 10, pp. 14780–14789, Dec. 2015.

[67] **R. V. Kurahatti, A. O. Surendranathan, A. V. R. Kumar, C. S. Wadageri, V. Auradi, and S. A. Kori**, "Dry Sliding Wear Behaviour of Epoxyreinforced with nanoZrO2 Particles," *Procedia Mater. Sci.*, vol. 5, pp. 274–280, 2014.